Theor. Comput. Fluid Dyn.
DOI 10.1007/s00162-007-0041-6

ORIGINAL ARTICLE

J. Dufek · **G. W. Bergantz**

Suspended load and bed-load transport of particle-laden gravity currents: the role of particle–bed interaction

Received: 1 May 2006 / Accepted: 2 November 2006

Abstract The development of particle-enriched regions (bed-load) at the base of particle-laden gravity currents has been widely observed, yet the controls and relative partitioning of material into the bed-load is poorly understood. We examine particle-laden gravity currents whose initial mixture (particle and fluid) density is greater than the ambient fluid, but whose interstitial fluid density is less than the ambient fluid (such as occurs in pyroclastic flows produced during volcanic eruptions or when sediment-enriched river discharge enters the ocean, generating hyperpycnal turbidity currents). A multifluid numerical approach is employed to assess suspended load and bed-load transport in particle-laden gravity currents under varying boundary conditions. Particle-laden flows that traverse denser fluid (such as pyroclastic flows crossing water) have *leaky* boundaries that provide the conceptual framework to study suspended load in isolation from bed-load transport. We develop leaky and saltation boundary conditions to study the influence of flow substrate on the development of bed-load. Flows with saltating boundaries develop particle–enriched basal layers (bed-load) where momentum transfer is primarily a result of particle–particle collisions. The grain size distribution is more homogeneous in the bed-load and the saltation boundaries increase the run-out distance and residence time of particles in the flow by as much as 25% over leaky boundary conditions. Transport over a leaky substrate removes particles that reach the bottom boundary and only the suspended load remains. Particle transport to the boundary is proportional to the settling velocity of particles, and flow dilution results in shear and buoyancy instabilities at the upper interface of these flows. These instabilities entrain ambient fluid, and the continued dilution ultimately results in these currents becoming less dense than the ambient fluid. A unifying concept is energy dissipation due to particle–boundary interaction: leaky boundaries dissipate energy more efficiently at the boundary than their saltating counterparts and have smaller run-out distance.

Keywords Particle-laden gravity current · Multiphase flow · Pyroclastic flows · Bed-load

PACS 91.40.Zz, 91.45.Wa, 91.50.Jc

Communicated by H. J. S. Fernando.

J. Dufek (✉)
Department of Earth and Planetary Science, University of California,
Berkeley, 307 McCone Hall, Berkeley, CA 94709, USA
E-mail: dufek@berkeley.edu

G. W. Bergantz
Department of Earth and Space Science, University of Washington,
Box 351310, Seattle, WA 98195, USA

List of Symbols

$^{m}c_i$	instantaneous velocity of mth phase [m/s]
$^{m}C_i$	fluctuating velocity of mth phase [m/s]
$C_{1\mu}$	constant in fluid turbulence model (0.09)
$C_{1\varepsilon}$	constant in fluid turbulence model (1.44)
$C_{2\varepsilon}$	constant in fluid turbulence model (1.92)
$C_{3\varepsilon}$	constant in fluid turbulence model (1.22)
C_{D}^{S}	drag coefficient
$^{m}c_{\mathrm{p}}$	heat capacity [J/kg K]
^{p}d	particle diameter [m] (1.0×10^{-4} m and 0.01 m)
e	restitution coefficient (0.65)
$^{m}e_{ij}$	strain rate [s^{-1}]
F_c	coefficient of friction (0.62)
g_i	gravitational acceleration [$\mathrm{m/s^2}$] (9.81 $\mathrm{m/s^2}$)
g_0	radial distribution function
H_{gp}	interphase heat transfer [$\mathrm{W/m^3}$]
H_1	hindrance coefficient in particle–particle drag (0.3)
$^{m}I_i$	interphase momentum transfer [$\mathrm{kg/m^3 s}$]
$^{p}I_{2\mathrm{D}}$	second invariant of rate of strain tensor [s^{-2}]
^{1}k	fluctuating kinetic energy of the gas phase [$\mathrm{m^2/s^2}$]
^{m}P	pressure [Pa]
^{m}q	thermal heat flux [$\mathrm{J/m^2 s}$]
R_{km}	ratio thermal conductivities
^{m}T	thermal temperature [K]
$^{m}U_i$	average velocity [m/s]
$^{m}\alpha$	volume fraction of mth phase
$^{m}\varepsilon$	dissipation rate of fluctuating kinetic energy [$\mathrm{m^2/s^3}$]
$^{p}\kappa$	granular conductivity [$\mathrm{J\ s/m^3}$]
$^{p}\theta$	granular temperature [$\mathrm{m^2/s^2}$]
$^{m}\mu$	dynamic viscosity [Pa s]
$^{m}\lambda$	bulk viscosity [Pa s]
$^{p}\varphi$	angle of internal friction (32°)
Π	turbulence exchange terms
$^{m}\rho$	density of mth phase [$\mathrm{kg/m^3}$]
σ_k	gas turbulence constant (1.0)
σ_ε	gas turbulence constant (1.3)
$^{m}\tau_{ij}$	stress tensor [Pa]

Preceding superscripts

$m = 1, 2, 3$ (1 is gas phase, and 2 and 3 are particle phases)
$p = 2$ and 3 (particle phases)

Subscripts

$i, j = 1, 2$ (indices for spatial direction)

1 Introduction

Particle-laden gravity currents are generated in a number of natural settings including volcanic eruptions, avalanches, and turbidity currents. Industrial accidents and explosions also have the potential to generate small-scale particulate flows. Hence, understanding the dynamics of these flows is essential in mitigating a wide range of environmental hazards. These flows are mixtures of particles with a carrier fluid (water or gas), and the mixture has a greater density than the surrounding, particle-less, ambient fluid. Consequently, these flows spread horizontally from their source, close to the ground. However, the interstitial fluid in many particle-laden gravity currents is less dense than the ambient fluid (i.e., interstitial hot gas in pyroclastic flows or fresh water in hyperpycnal turbidity currents). Hence, portions of the flow that become sufficiently dilute in the particle phase will undergo a buoyancy reversal. A substantial amount of research has been conducted on gravity currents [1–6] although much of it has focused on homogenous fluids of two densities to create the current. The Lagrangian, or local physics of particulate multiphase flows cannot be resolved by this approach. For example, the heterogeneous concentration of particles during an ongoing flow, the phase-relative motion, and dilution from particle deposition, are added complications that lead to emergent time and length scales in particle-laden flows.

An important class of particle-laden gravity currents are those that traverse a much denser *fluid*. Examples include pyroclastic flows from volcanic eruptions and avalanches (granular and powder snow) that encounter lakes or oceans. A number of volcanic events near large bodies of water have resulted in numerous eruptions producing over-water pyroclastic flows [7–10]. Real-time accounts of a few of these eruptions [7] and deposits from others [9] indicate that a substantial amount of material can be transported great distances over water. For instance, flows from Krakatau were reported 60 km from the source, and flows from the Kos, Greece eruption produced deposits >40 km from their source [7,9]. Understanding the frequency and dynamics of these events is hampered due to the fact that deposits from these eruptions are often submerged, and observations are sparse.

Analogue experiments [11] have elucidated several features of over-water particulate gravity currents, including the bifurcation of some flows into below-water turbidity currents and more-dilute over-water flows. However, there are a number of scaling issues that hinder the application of these experiments to natural events. For example, it is difficult to produce high-Reynolds-number experimental flows. The particle response time due to fluid forcing observed in natural flows (i.e., Stokes number) is also rarely matched in experimental flows [12]. In addition, detailed optical measurements of real-time particle concentration in analogue experiments are limited to dilute flows (less than ∼3 vol % [13].

The controls on the partitioning of particle mass into the dilute upper regions of a flow versus dense basal regions are poorly known in particle-laden gravity currents. The relative importance of bed-load (where particles make multiple contacts with the bottom boundary) and suspended load (where particles are suspended primarily due to turbulence) is difficult to distinguish from deposits generated by flows that have traversed opaque boundaries (over land). However, most (if not all) of the bed-load of flows that traverse a leaky (over-water) boundary will be removed. Hence this natural filter enables the study of suspended load transport in relative isolation and should allow for estimates of the relative proportion of over-land pyroclastic flows that are being transported by suspension due to grain collisions and turbulence.

Due to the experimental scaling difficulty, we have adopted a multiphase numerical approach to elucidate the spatial and temporal heterogeneity that develops in particle-laden gravity currents. In this Eulerian–Eulerian approach, multiple particle species are treated as distinct, but interpenetrating, continua and grading and segregation of particle size and volume fraction are calculated [14]. One novel aspect of this work is the development of a leaky boundary condition utilizing a reconstruction of the local particle velocity probability distribution in order to study flows without bed-load. For comparison a *saltation* boundary condition is developed in which particles interact collisionally with the basal substrate. Using these contrasting boundary conditions we evaluate the mass and energy transport of particle-laden gravity currents. In particular we examine the relative importance of bed-load on mass flux and run-out of particle-laden flows.

This paper is organized as follows. In Sect. 2 a multiphase continuum model is developed for a bimodal particle size population along with a framework for the scaling analysis employed. Section 3 derives leaky and saltation boundary conditions using the mean and fluctuating components of the particle velocity field. Section 4 describes the simulation conditions. Section 5 describes the results of the numerical simulations. These results reveal the consequences of phase-relative motion for both saltation and leaky boundaries and resulting instabilities. The relative importance of a basally concentrated zone on flow transport is emphasized. Finally in Sect. 6 we discuss the dynamics and structure of particle-laden gravity currents in the context of this numerical experiment, and compare the results to previous approximations employed to study their transport.

2 Continuum multiphase model

Continuum multiphase models, initially developed in the fields of chemical and nuclear engineering [15–18] have shown promise in their ability to predict the mesoscale clustering of particles in turbulent suspensions, and similar approaches have been applied to volcanic eruptions [19–21]. In the multifluid approach each particle phase and the carrier fluid phase has separate conservation equations for momentum, mass, and energy along with closure assumptions for heat and momentum transfer within and between phases (summarized in Table 1 and in the Appendix).

Table 1 Multifluid equations

Mean field equations

$$ {}^{m}c_i = \left\langle {}^{m}c_i \right\rangle + {}^{m}C_i = {}^{m}U_i + {}^{m}C_i \tag{1} $$

$$ \sum {}^{m}\alpha = 1, \tag{2} $$

Continuity

$$ \frac{\partial}{\partial t}\left({}^{m}\alpha\,{}^{m}\rho\right) + \frac{\partial}{\partial x_i}\left({}^{m}\alpha\,{}^{m}\rho\,{}^{m}U_i\right) = 0, \tag{3} $$

Momentum

$$ \frac{\partial}{\partial t}\left({}^{m}\alpha\,{}^{m}\rho\,{}^{m}U_i\right) + \frac{\partial}{\partial x_j}\left({}^{m}\alpha\,{}^{m}\rho\,{}^{m}U_i\,{}^{m}U_j\right) = -\frac{\partial\,{}^{m}P}{\partial x_i}\delta_{ij} + \frac{\partial\,{}^{m}\tau_{ij}}{\partial x_j} + {}^{m}I_i + {}^{m}\alpha\,{}^{m}\rho g_i, \tag{4} $$

Thermal Energy

$$ {}^{m}\alpha\,{}^{m}\rho\,{}^{m}c_p\left(\frac{\partial\,{}^{m}T}{\partial t} + {}^{m}U_j\frac{\partial\,{}^{m}T}{\partial x_j}\right) = -\frac{\partial\,{}^{m}q}{\partial x_i} + H_{gp}. \tag{5} $$

Fluctuating field equations

Turbulent kinetic energy, fluid phase

$$ {}^{1}k = \frac{1}{2}\left\langle {}^{1}C_i\,{}^{1}C_i \right\rangle, \tag{6} $$

Turbulent kinetic energy equation, fluid phase

$$ {}^{1}\alpha\,{}^{1}\rho\left(\frac{\partial\,{}^{1}k}{\partial t} + {}^{1}U_j\frac{\partial\,{}^{1}k}{\partial x_j}\right) = \frac{\partial}{\partial x_i}\left({}^{1}\alpha\frac{{}^{1}\mu^{t}}{\sigma_k}\frac{\partial\,{}^{1}k}{\partial x_i}\right) + {}^{1}\alpha\,{}^{1}\tau_{ij}\frac{\partial\,{}^{1}U_i}{\partial x_j} + \Pi_{k1} - {}^{1}\alpha\,{}^{1}\rho\,{}^{1}\varepsilon, \tag{7} $$

Dissipation rate of kinetic energy, fluid phase

$$ {}^{1}\alpha\,{}^{1}\rho\left(\frac{\partial\,{}^{1}\varepsilon}{\partial t} + {}^{1}U_j\frac{\partial\,{}^{1}\varepsilon}{\partial x_j}\right) = \frac{\partial}{\partial x_i}\left({}^{1}\alpha\frac{{}^{1}\mu^{t}}{\sigma_\varepsilon}\frac{\partial\,{}^{1}\varepsilon}{\partial x_i}\right) + {}^{1}\alpha\frac{{}^{1}\varepsilon}{{}^{1}k}\left(C_{1\varepsilon}\,{}^{1}\tau_{ij}\frac{\partial\,{}^{1}U_i}{\partial x_j} - {}^{1}\rho C_{2\varepsilon}\,{}^{1}\varepsilon\right) + \Pi_{\varepsilon 1}, \tag{8} $$

Pseudo-thermal equation, particle phases

$$ {}^{p}\alpha\,{}^{p}\rho\left(\frac{\partial\,{}^{p}\theta}{\partial t} + {}^{p}U_j\frac{\partial\,{}^{p}\theta}{\partial x_j}\right) = \frac{\partial}{\partial x_i}\left({}^{p}\alpha\,{}^{p}\rho\,{}^{p}\kappa\frac{\partial\,{}^{p}\theta}{\partial x_i}\right) + {}^{p}\alpha\,{}^{p}\rho\,{}^{p}\tau_{ij}\frac{\partial\,{}^{p}U_i}{\partial x_j} + \Pi_{k2} - {}^{p}\alpha\,{}^{p}\rho\,{}^{p}\varepsilon. \tag{9} $$

Preceding superscripts: m=1, 2, 3 (1 is gas phase, and 2 and 3 are particle phases) s, p=2 and 3 (particle phases); subscripts: i, j = 1, 2 (indices for spatial direction)

Both the mean and fluctuating velocities are calculated for the granular and fluid phases. For the simulations in this study we have adapted the MFIX multiphase code for use on saltating and leaky boundary condition flows [22] (Fig. 1).

It is instructive to render the continuity, momentum and energy equations in Table 1 dimensionless. We define the following dimensionless parameters indicated by the prime superscript: nondimensional density,

$$ \rho' = \frac{\rho}{\rho_{\mathrm{amb}}}, \tag{10} $$

where ρ_{amb} is the ambient, initial gas density, nondimensional pressure

$$ P' = \frac{P}{P_0}, \tag{11} $$

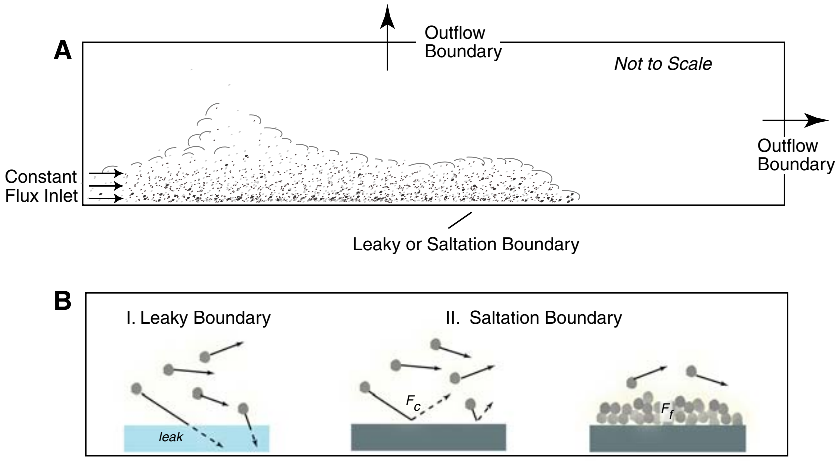

Fig. 1 Schematic representation of: **A** simulation conditions and **B** boundary conditions. **A** The particle-laden gravity currents are introduced at constant flux from the left boundary and propagate to the right. *Top* and right side are outflow boundaries, and the basal boundary reflects either a leaky condition or a saltating condition. **B** For leaky boundaries, the leak flux is calculated at every time-step based on a reconstruction of the local particle velocity probability distribution. Particles interact with the saltating boundaries through inelastic collisions and frictionally

where P_0 is the initial gas pressure at the bottom boundary, a nondimensional velocity

$$U' = \frac{U}{U_0}, \tag{12}$$

where U_0 is the initial inlet velocity, a nondimensional temperature normalized by the initial ambient temperature

$$T' = \frac{T}{T_0}, \tag{13}$$

and a nondimensional shear and bulk viscosity

$$\mu' = \frac{\mu}{\mu_0}, \tag{14}$$

and

$$\lambda' = \frac{\lambda}{\mu_0}, \tag{15}$$

normalized by the initial gas viscosity. We define a length scale normalization H^* based on the observation that densimetric Froude numbers of approximately 1–1.4 have been measured in experiments [2,23] where the densimetric Froude number is defined as

$$Fr_{\mathrm{d}} = \frac{U}{\sqrt{g^* H}}, \tag{16}$$

where g^* is the reduced gravity ($g^* = \frac{\rho_{\mathrm{mix}} - \rho_{\mathrm{amb}}}{\rho_{\mathrm{amb}}} g$) and H is the gravity current height. Based on these experiments, a Froude number of unity will be used for reference in these simulations, so that

$$H^* = U_0^2 / g^*. \tag{17}$$

While the emergent Froude number, based on the local velocity and particle concentration, can and does deviate from unity, we use this as our reference state in the definition of our length scale normalization. Following from this definition the dimensionless length scale is

$$x' = \frac{x}{H^*}, \tag{18}$$

and the dimensionless fluid time scale is

$$t' = \frac{tU_0}{H^*}. \tag{19}$$

In the following analysis we compare the fluid timescale,

$$\tau_{\mathrm{f}} = \frac{H^*}{U_0}, \tag{20}$$

to the aerodynamic response time of the particle phase (τ_{p}), the characteristic timescale of dispersal of thermal energy from the particle phase to the fluid (τ_{T}), and a settling timescale ($\tau_{0.5}^{S}$). The aerodynamic response time of the particle phase is given as

$$\tau_{\mathrm{p}} = \frac{4V_{\mathrm{r}}\left({}^{p}d\right)}{3\Delta u\left({}^{1}\rho'\right)\left({}^{1}\alpha\right)\left({}^{p}\alpha\right)C_{\mathrm{D}}}, \tag{21}$$

where V_{r} is the ratio of the terminal velocity of a group of particles to the single particle terminal velocity (Appendix Eq. A20), Δu is the difference in the velocity of the particle and fluid phases, and C_{D} is the drag coefficient [24,25]. The timescale for the transmission of thermal energy from the dispersed phase to the continuous phase is

$$\tau_{\mathrm{T}} = \frac{\left({}^{p}d\right)^{2}\left({}^{1}\rho\right)c_{\mathrm{p}}}{6\left({}_{\mathrm{Th}}^{1}k\right)\left(1-{}^{1}\alpha\right)Nu}, \tag{22}$$

where Nu is an empirical Nusselt number correlation (Appendix Eq. A57) and ${}_{\mathrm{Th}}^{1}k$ is the thermal conductivity of the gas phase. Finally, we will also make use of reference time and length scales based on the settling of particles under gravity. If a particle–fluid suspension is well mixed, and particle–particle interactions are negligible, the particle volume fraction in the flow is expected to follow an exponential relation as a result of loss by sedimentation [26,27], with the decay constant reflecting the height of the flow and the settling velocity:

$$\frac{{}^{p}\alpha}{{}^{p}\alpha^{0}} \propto \mathrm{e}^{-(w_{\mathrm{s}}/H^*)t}, \tag{23}$$

where ${}^{p}\alpha$ is the particle volume fraction, ${}^{p}\alpha^{0}$ is the initial particle volume fraction, w_{s} is the particle settling velocity, and H^* is the scale height of the flow. We define a decay half-life of the flow to be the time at which the concentration in the flow decays to half the initial concentration. We also define $L_{0.5}$ as the product of the inlet velocity and the particle half-life and use this as our reference horizontal settling length scale so that our dimensionless time and length settling scales are

$$\tau_{0.5}^{\mathrm{S}} = \frac{-(H^*)\ln(0.5)}{w_{\mathrm{s}}}, \tag{24}$$

$$t_{\mathrm{s}}' = t/\tau_{0.5}^{\mathrm{S}}, \tag{25}$$

and

$$L' = L/L_{0.5}. \tag{26}$$

The length scale $L_{0.5}$ can be interpreted as the horizontal distance at which half the particles in the flow will have been sedimented, if the only force acting on the particles is settling under gravity.

Using the above dimensionless quantities the continuity, momentum and thermal energy equations become

$$\frac{\partial}{\partial t'}\left({}^{m}\alpha^{m}\rho'\right) + \frac{\partial}{\partial x_i'}\left({}^{m}\alpha^{m}\rho'^{m}U_i'\right) = 0, \tag{27}$$

$$\begin{aligned}\frac{\partial\left({}^{m}\alpha^{m}\rho'^{m}U_i'\right)}{\partial t'} + \frac{\partial\left({}^{m}\alpha^{m}\rho'^{m}U_i'^{m}U_j'\right)}{\partial x_i'} &= \left[\frac{{}^{m}N}{{}^{m}M_0^2}\right]\frac{\partial\left({}^{m}P'\right)}{\partial x_i'} + \left[\frac{1}{Re}\right]\frac{\partial}{\partial x_i'}\left[{}^{m}\tau_{ij}'\right] \\ &\quad + \left[\frac{1}{St}\right]\left({}^{1}U_i' - {}^{p}U_i'\right) + \left[\frac{1}{Fr_{\mathrm{d}}^2}\right]\alpha\hat{e}_g,\end{aligned} \tag{28}$$

$${}^{m}\alpha^{m}\rho'^{m}c_p'\left[\frac{\partial^{m}T'}{\partial t'} + {}^{m}U_i'\frac{\partial^{m}T'}{\partial x_i'}\right] = \left[\frac{1}{Pe}\right]\frac{\partial^{m}q'}{\partial x_i'} + \left[\frac{1}{{}^{\mathrm{Th}}St}\right]\left(T_{\mathrm{p}}' - T_{\mathrm{f}}'\right). \tag{29}$$

Table 2 Particle scaling

Name	$< u^* >^a$	${}^1St^b$	${}^2St$	${}^1Pn^c$	${}^2Pn$	${}^1\Sigma_T^d$	${}^2\Sigma_T$	${}^{1,\mathrm{Th}}St^e$	${}^{2,\mathrm{Th}}St$
1L	1.9	0.0014	7.4	0.78	49.60	3.7e−4	1.9	1.7×10^{-3}	3.8×10^{-3}
2L	2.8	0.0014	7.4	0.53	33.66	3.7e−4	1.9	4.1×10^{-4}	3.7×10^{-3}
3L	3.3	0.00065	4.3	0.45	28.56	8.9e−5	0.58	1.6×10^{-3}	3.6×10^{-3}
4L	3.6	0.00065	4.3	0.42	26.18	8.9e−5	0.58	3.9×10^{-4}	3.5×10^{-3}
1S	2.3	0.0014	7.4	0.65	40.97	3.7e−4	1.9	1.7×10^{-3}	3.8×10^{-3}
2S	3.2	0.0014	7.4	0.47	29.45	3.7e−4	1.9	4.1×10^{-4}	3.7×10^{-3}
3S	5.4	0.00065	4.3	0.28	17.45	8.9e−5	0.58	1.6×10^{-3}	3.6×10^{-3}
4S	5.6	0.00065	4.3	0.27	16.83	8.9e−5	0.58	3.9×10^{-4}	3.5×10^{-3}

[a] Shear velocity

[b] Particle Stokes number, the number superscript refers to the two different particle phases

[c] Particle Rouse number, the number superscript refers to the two different particle phases; the Rouse number is discussed in Sect. 6.2 to compare these calculations to a Roussean approximation

[d] Particle stability number, the number superscript refers to the two different particle phases

[e] Particle thermal Stokes number, the number superscript refers to the two different particle phases

Table 3 Simulation conditions

Name	BC	${}^p\alpha^a$	Velocity (m/s)	VF^b	H^*	$Fr_{\mathrm{d}}^{0\ddagger}$	Re	Pe	${}^1M_0$
1L	L	0.025	50	12.5	66.5	0.62	2.4×10^8	5.7×10^{-9}	0.15
2L	L	0.10	50	50	66.5	0.31	2.4×10^8	5.7×10^{-9}	0.15
3L	L	0.025	100	25	137.9	1.23	1.0×10^9	1.4×10^{-9}	0.30
4L	L	0.10	100	100	137.9	0.62	1.0×10^9	1.4×10^{-9}	0.30
1S	S	0.025	50	12.5	66.5	0.62	2.4×10^8	5.7×10^{-9}	0.15
2S	S	0.10	50	50	66.5	0.31	2.4×10^8	5.7×10^{-9}	0.15
3S	S	0.025	100	25	137.9	1.23	1.0×10^9	1.4×10^{-9}	0.30
4S	S	0.10	100	100	137.9	0.62	1.0×10^9	1.4×10^{-9}	0.30

Boundary conditions: L leaky boundary, S saltation boundary

[a] Solid volume fraction

[b] Solids volume flux (m^3/s)

Dimensional analysis of the momentum equation utilized the equation of state for the gas (ideal gas) and for a granular material (see Appendix). Specifically, the ${}^mN$ term is dependent on the equation of state of the material, and for the gas phase is dependent on the ratio of the heat capacities at constant volume and constant pressure. For granular materials, ${}^mN$ is dependent of the volume fraction of particles and the coefficient of restitution (Appendix Eqs. A60, A64).

The thermal energy equation has two dimensionless parameters, the Peclet number (Pe) and a thermal Stokes number (${}^{\mathrm{Th}}St$). The Peclet number is a measure of the heat transported by convection relative to heat transport by conduction:

$$Pe = \frac{{}^{1}_{\mathrm{Th}}\kappa}{H^* U_0}, \tag{30}$$

where ${}^{1}_{\mathrm{Th}}\kappa$ is the thermal diffusivity of the gas phase. The thermal Stokes number is a ratio of the timescale of transfer of thermal energy from the dispersed phase to the fluid phase relative the timescale of fluid motion referred to previously (Eqs. 20, 22):

$${}^{\mathrm{Th}}St = \frac{\tau_{\mathrm{T}}}{\tau_f}. \tag{31}$$

Initial Peclet and thermal Stokes numbers are given in Tables 2 and 3.

The momentum equation has four dimensionless terms that govern the advection of material: the Mach number (${}^{\mathbf{m}}M_0$), the Reynolds number (Re), the Stokes number (St), and the Froude number (Fr_{d}). The Mach number is the ratio of the phase velocity to its speed of sound,

$${}^m\mathbf{M}_0 = \frac{U_0}{{}^m a}, \tag{32}$$

and the Reynolds number is the ratio of the inertial to viscous forces,

$$Re = \frac{\rho_0 U_0 H^*}{\mu_0}. \tag{33}$$

To describe momentum transfer in these flows, and emergent instabilities, we will employ the Stokes number (St), and stability factor (Σ_T), and the gradient Richardson number (Ri). The Stokes number indicates the particle response time scale relative to the time with which the particle interacts with the flow [28,29]:

$$St = \frac{\tau_\mathrm{p}}{\tau_\mathrm{f}}. \tag{34}$$

The large-eddy Stokes number for each particle size and for each flow condition is given in Table 2.

The interplay of steady forcing (gravity) and unsteady forcing (turbulent drag and particle–particle interaction) will impact the segregation or dispersal of particles. The Stokes number is a measure of the unsteady forcing due to particle–fluid drag, and the Froude number scales with the gravitational forcing. The ratio $\frac{St}{Fr^2}$, which we will refer to as the stability factor (Σ_T), is a measure of the relative importance of these forcings on the particle phase [29,30]. As emphasized by Raju and Meiburg [29] steady forcing such as gravity cannot inherently create phase-relative segregation, and particles with large stability factor are more evenly distributed when interacting with vortical structures compared to small stability factor particles. As the smaller stability factor particles couple with vortical structures they are also more readily suspended and sediment at a lower rate [29].

The gradient Richardson number is a measure of the stability of stratified flow (in this case stratified vertically in particle volume fraction) compared to destabilizing shear due to the flow of these gravity currents. The gradient Richardson number is given by

$$Ri = \frac{(-g/\rho_\mathrm{amb})\,(\partial\rho_\mathrm{mix}/\partial y)}{(\partial U/\partial y)^2}. \tag{35}$$

Here we define ρ_mix as the average of the particle and fluid density, although we stress that the particle and fluid transport are solved with separate equations, and ρ_mix evolves in space and time. Flows with gradient Richardson numbers greater than 0.25 typically are stable (the density gradient is sufficiently great that the shear cannot overcome the stratification), whereas small- or negative-gradient Richardson numbers have unstable density gradients that promote the development of Kelvin–Helmholtz instabilities, and the entrainment of the surrounding ambient fluid.

Constitutive relations are required to close the momentum and thermal energy equations. These constitutive relations were chosen to match the conditions likely to occur in turbulent, particle-laden pyroclastic density currents. For collisional transfer of momentum, the constitutive relation for the particle phase is provided by kinetic theory similar to that used in the estimation of gas viscosities from molecular collisions [20,31]. This constitutive relation assumes binary, inelastic particle collisions. The collision rate and stress in the granular material depends on the fluctuating particle velocity. A separate transport equation for pseudo-thermal energy is solved to determine the granular temperature (covariance of the fluctuating velocity) and close the granular stress in dilute conditions. Pseudo-thermal energy is assumed to be advected by the mean flow and diffuses along gradients in the granular temperature. Locally pseudo-thermal energy is produced by shear and by the relative velocity between the particle and gas phases [18] and is dissipated by inelastic collisions and by viscous damping by the carrier fluid. The production of fluctuating motions by gas–particle slip and dissipation by viscous forces ensures that the granular pseudo-thermal energy equation is coupled to the carrier fluid. A similar constitutive model was used by Benyahia et al. [32] in turbulent, particle-laden pipe flow and good agreement was achieved between their simulations and the experiments of Jones [33].

At higher particle volume fractions, protracted frictional interaction of particles occurs and the frictional and collisional stresses are assumed to be additive [34,35]. The frictional stress is developed using the postulate of a yield function and an associated flow-rule to relate stress and strain rate, and has been adopted from theories of soil mechanics. The solids pressure in the frictional regime allows the solid phases to have some compressibility, but provides a resisting force to prevent unphysical void fractions. In the limit of volume fractions approaching the minimum void fraction both the frictional pressure and granular shear viscosity approach infinity, which prevents further circulation of material.

A modified k–ε turbulence model proposed by Simonin is used to predict the Reynolds stresses produced by fluctuating fluid motion [32,36]. This approach accounts for production and dissipation of turbulent energy

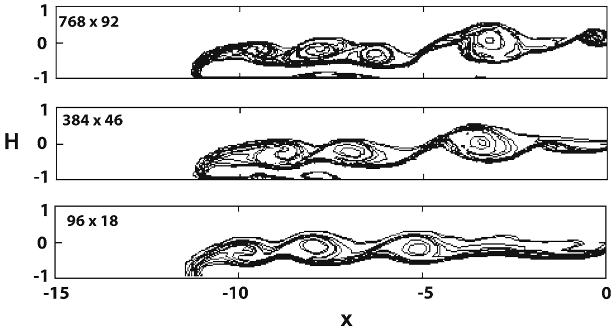

Fig. 2 Comparison of lock-exchange gravity current at different grid resolution (768 × 92, 384 × 46 and 96 × 18) at time = 20. The boundaries are no-slip and the lock-exchange configuration and units are equal to those used in Hartel et al. A density ratio of $\rho_2 - \rho_1/\rho_{\text{avg}} = 0.36$ was used to achieve similarity of Reynolds number ($\sim$710) compared to the experiments of Hartel et al. This figure is directly comparable to Fig. 3 of the Hartel et al. study, and the front velocity is within 1% of the DNS front velocity

due to the presence of a dispersed phase [37]. Hence the random, or fluctuating motion of the continuous phase and the dispersed phase are two-way coupled. In this two-equation turbulence model separate transport equations are formed for the turbulent (fluctuating) kinetic energy of the continuous phase and for the dissipation rate of kinetic energy. The standard turbulent kinetic energy equation (Eq. 7) and dissipation rate equation (Eq. 8) are modified by source terms to account for production and dissipation of turbulent energy as a result of particle loading [37]. These particle–fluid coupling terms will result in decreased turbulent production in the gas phase at higher particle concentrations, as was demonstrated by Benyahia et al. [32]. Hence, in regions of particle stratification the flow will be stabilized against the large production of turbulent energy due to shear. Wall functions and modifications for the near-boundary production and dissipation were implemented for the near-wall laminar boundary layer. References [32,37,38] provide a thorough review of the two-way coupled approach to fluctuating granular and turbulent motion, and the reader is referred to these references for a detailed discussion of this approach. Again, this approach and model constants were validated by Benyahia et al. [32] through comparison with experiments of particle-laden flows [33].

We conducted several other validation tests to evaluate this turbulent multiphase approach for particle-laden gravity currents, including comparing the results to well-established direct numerical simulation results. Hartel et al. [3] conducted a direct numerical simulation (DNS) of two fluid density currents in a lock-exchange configuration with both free-slip and no-slip boundary conditions [3]. We repeated their two-dimensional (2D) simulations (Figs. 3, 11 in Hartel et al.) with different grid resolutions using the Simonin k–ε formulation. The original DNS of Hartel et al. was single phase (fluid) and we mimicked this by setting the Stokes number of the particle phase to very small values (so the particles behaved as tracers for the fluid motion) and seeded the particles such that the density variation between the two fluids was the same as in the Hartel et al. numerical experiment. Selected results at different grid resolutions are shown in Figs. 2 and 3. For both the free-slip and no-slip cases the gravity current front velocity was within 1% of the DNS results of Hartel et al. [3] for all resolutions tested. The details of the Kelvin–Helmholtz instabilities are different at lower resolution (small-scale features fail to be resolved) although horizontally averaged densities remain comparable at 1/8 the resolution used in Hartel et al. Lowe et al. [39], compared the results of intrusive gravity current experiments with the DNS of Hartel et al. with generally good agreement, although Kelvin–Helmholtz billows in the DNS of Hartel et al. were higher amplitude than in the experiments because the two-dimensional geometry of the DNS did not allow for the three-dimensional breakdown of these turbulent structures. The distance that billows appear behind the front of the head (x/H) in the k–ε simulations is $\sim$1.25–3.0, which compares well with the distance measured by Lowe et al. [39] of 1.5–2.5. Both of these results are somewhat lower than the two-dimensional DNS of Hartel et al. which had x/H of 2.5–4.0.

The thermal energy of the flow is described by a transport equation (Eq. 29) which includes the effect of advection, conduction and interphase transfer of enthalpy. In order to simplify this analysis viscous dissipation and radiative transfer of heat were not considered [40]. We also assume that heat transfer between different solid phases is negligible. The fluid–solid heat transfer coefficient is a function of the local Nusselt number, which reflects the ratio of convective heat transfer to conductive heat transfer. The Nusselt number depends on the local particle volume fraction, Reynolds number and Prandtl number as reflected in the empirical correlation (A57) [41]. The Nu number correlation is based on the experiments of Gunn [41] which included dense to dilute flow (particle volume fraction (0.4–1.0) and Reynolds numbers in excess of 10^5.

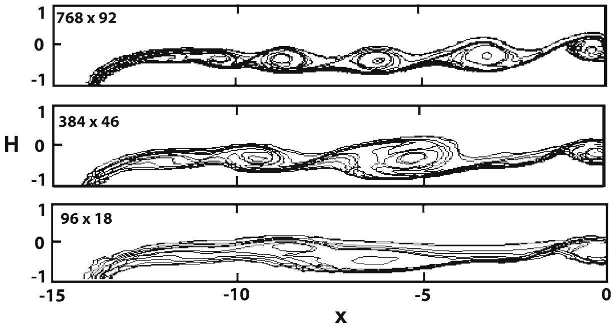

Fig. 3 Comparison of lock-exchange gravity current using free-slip boundaries at different grid resolution (768 × 92, 384 × 46 and 96 × 18) at time = 20. The front velocity is again within 1% of the Hartel et al. DNS values and the structure of the head compares well with the DNS result. The horizontally averaged density is similar between the different resolutions although the structure of the Kelvin–Helmholtz instabilities are not preserved as well at lower resolution

A binary mixture of two different particle sizes was used in the simulations in order to assess size sorting in the simplest possible multi-particle system. Drag between particle phases is based on kinetic theory [16] but modified by a hindrance term proposed by Gera et al. to account for protracted contact between particle phases as close packing is approached (preventing phase-relative circulation at close-packing) [14]. Likewise the radial distribution function must be modified according to the proportion and sizes of the different particle phases [42].

3 Boundary conditions for leaky and saltation boundaries

In multiphase flows, separate boundary conditions must be specified for the continuous and particle phases. At a rigid, stationary boundary a common approach is to invoke a no-slip boundary for the continuous or gas phase, while the particle phases are modeled as a saltation or partial-slip boundary [43]. The shear associated with the particle–wall interactions is a product of the collisional frequency, the tangential momentum transfer per collision, and the concentration of particles near the wall (Eq. 36):

$$F_c = \overbrace{\frac{(3\theta)^{1/2}}{s}}^{\text{collisional frequency}} \times \overbrace{\frac{\phi\pi\rho_{\mathrm{p}}d^3(U_{\mathrm{p}}-U_{\mathrm{w}})}{6}}^{\text{tangential momentum transfer/collision}} \times \overbrace{\frac{1}{a_c}}^{\text{number of particles}}, \tag{36}$$

where ϕ is the specularity (the fraction of tangential momentum transferred, which depends on the surface roughness), θ is the granular temperature, s is the average distance between the wall and particle, and a_c is the boundary area/particle. In the simulations presented here the specularity coefficient was held constant at 0.02 for consistency [32], although under natural conditions the specularity coefficient is likely to vary significantly over different surface conditions. Averaged over many particles to form the continua, this relation becomes

$$F_c = \frac{{}^{p}\alpha g_0(3\theta)^{1/2}\phi\pi({}^{p}\rho)(U_{\mathrm{p}}-U_{\mathrm{w}})}{6\,{}^{p}\alpha^0}, \tag{37}$$

where g_0 is the radial distribution function (A27), and ${}^{p}\alpha^0$ is the solid volume fraction at close packing. This collisional force is converted into a condition for the particle phase velocity gradient and permits nonzero velocities at the boundary. The fluctuating kinetic energy of the granular phase is also dissipated at the boundary due to inelastic collisions as specified in the granular conductivity equation (A28) [43].

This saltation condition is imposed at the boundary by calculating the velocity gradient and using a ghost cell method, so that

$$\mu\frac{\partial u}{\partial y} = F_c. \tag{38}$$

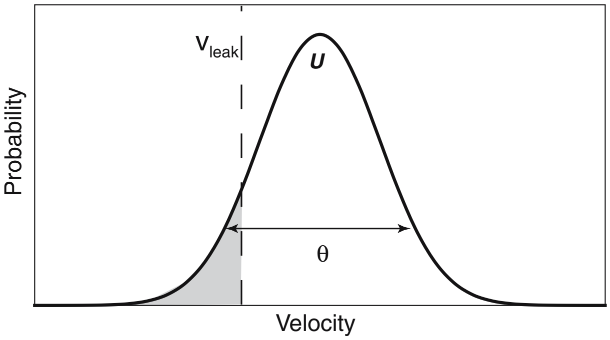

Fig. 4 Example of a reconstructed velocity probability distribution. Both the mean velocity and granular temperature are shown. All velocities below the leak velocity are capable of removing a particle from the flow, and integration of the shading region gives the flux of particles from the system over the given time step

Using the defined dimensionless parameters, along with

$$\theta' = \frac{\theta}{u_0^2}, \tag{39}$$

gives the following relation:

$$\frac{\partial U'}{\partial y'} = {}^{\mathrm{G}}Re \frac{{}^{p}\alpha g_0 (3\theta')^{1/2} \varphi \pi ({}^{p}\rho')(U'_{\mathrm{slip}})}{6 {}^{p}\alpha_{\mathrm{cp}}}, \tag{40}$$

where ${}^{\mathrm{G}}Re$ is the granular Reynolds number, ${}^{p}\alpha_{\mathrm{cp}}$ is the volume fraction of particles at close packing, and U'_{slip} is the dimensionless particle slip velocity at the boundary. The granular Reynolds number is defined as in Eq. 33, although using the granular viscosity.

3.1 Derivation of a leaky boundary condition from the velocity probability distribution

For the dynamics of a particle-laden gravity current interacting with a leaky boundary, we consider the end-member scenario in which all particles that reach the boundary are removed from the flow. In this way, only transport of the suspended load of the flow is considered. This is similar to considering the particles as being perfectly sticky (i.e., no possibility of saltation at the boundary).

Sedimentation from the flow requires consideration of both the mean and fluctuating component of a particle species' velocity field. The nonzero variance (i.e., granular temperature) of the velocity for a collection of particles can result in a finite sedimentation rate in regions of the flow where the mean vertical particle velocity component is zero or even positive. As demonstrated in Eq. (9) the granular temperature, and hence the particle velocity probability distribution, is influenced by collisions with other particles and drag with the fluid. Local variation in the sedimentation rate is dependent upon this velocity distribution and the concentration of particles near the boundary. To examine this effect we can define the leak velocity (v_{leak}) as the velocity sufficient to remove a particle from a given height in the flow during a time interval:

$$v_{\mathrm{leak}} = \frac{\bar{l}}{\Delta t}, \tag{41}$$

where $\bar{l}$ is the average distance to the boundary in a control volume and Δt is a time interval. In Fig. 4 an example leak velocity is plotted along with an example velocity probability distribution. All velocities less than the leak velocity are sufficient to cause sedimentation through the leaky boundary (shaded area in Fig. 4). Integration of the probability distribution from negative infinity to the leak velocity and multiplying this by volume fraction of particles gives the local finite flux of particles from the flow. Again assuming that the particle distribution is Maxwellian this gives the expression

$$\gamma = \frac{{}^{p}\alpha}{2} \left[1 + \operatorname{erf}\left(\frac{v_{\mathrm{leak}} - \bar{v}}{\sqrt{2\theta}} \right) \right], \tag{42}$$

where γ is the volume fraction loss rate over the computational time step. In dimensionless quantities, the fractional loss rate is given by

$$\gamma = \frac{{}^{p}\alpha}{2}\left[1 + \operatorname{erf}\left(\frac{v'_{\text{leak}} - \bar{v}'}{\sqrt{2\theta'}}\right)\right], \tag{43}$$

again using Eq. 39 for the dimensionless granular temperature.

4 Particle-laden gravity current conditions

4.1 Initial and boundary conditions

The simulation conditions are depicted in Fig. 1. A constant flux of particles and gas were introduced in these two-dimensional simulations and was varied to reflect different particle volume fractions and velocities (Table 3). In all simulations the gas and particles were introduced at 700 K into an atmosphere of 300 K. Gas density was determined using the perfect gas relation assuming a dry atmosphere. Hence the interstitial gas of these flows has a lower density than the ambient air; although the initial particle and gas mixture is denser than surrounding atmosphere. The top and side boundaries are outflow boundaries and the bottom boundary was either a saltation boundary (S) or a leaky boundary (L). The vertical grid spacing is refined at the base of the flow and increases with height (H' = 0.0125–0.075 H' or 1–6 m) and the horizontal resolution is $\sim$0.001 L' (6 m). The physical domain of these two-dimensional simulations is 573 m × 15 km. Initial solid volume fractions were either 0.025 or 0.1 in these simulations. Two grain sizes were used to assess sorting of different grain sizes and densities: 95% of the flow was comprised of ash with diameter of 1.125×10^{-4} m and density of 2,000 kg/m^3 and 5% of the flow was comprised of denser particles (lithics) with a diameter of 0.01 m and density of 2,700 kg/m^3. The smaller particle size corresponds to stability factors of much less than 1 ($\Sigma_{\mathrm{T}} \ll 1$, $St \ll 1$) whereas the larger and denser particles had stability factors of $\sim$1 ($\Sigma_T \sim 1$, $St \geq 1$) (Table 2).

5 Structure of particle-laden flows

Although the size and details of the flow structure are different for every simulation, several generic flow structures are common to all the simulations. The particle-laden gravity currents that traverse leaky boundaries are more dilute on average than the saltation boundary flows. The run-out distance (the furthest extent of the flow) in the leaky boundary flows is marked by the point at which enough particles have been lost that a buoyancy reversal occurs and the flows become lighter than the ambient fluid. In contrast, flows that traverse saltation boundaries develop a bed-load region enriched in particles. Bed-load particles eventually deposit, as energy is lost due to inelastic collisions. The particle residence time in the saltating flows is greater than in the leaky boundary situation and they produce longer run-out flows. In the following sections we will examine the heterogeneity that develops for the saltation and leaky boundaries and how sorting, energy content and mass flux are ultimately influenced by transport over the two substrates.

5.1 Density stratification

Gradients in the particle volume fraction develop due to the interaction of gravitational acceleration and the turbulent suspension of different size particles, resulting in a more particle-enriched base as the particle-laden flows continue to propagate away from the inlet (Fig. 5). The development of particle volume fraction gradients has important implications for entrainment, particle–particle interaction in the more concentrated regions of the flow, the development of bed-load for the saltating boundaries and particle loss at the leaky boundaries. Spatially averaged particle volume fractions and horizontal velocity are remarkably similar for both saltating and leaky boundaries in the upper regions of the flow (>10% of the scale height of the flow). In this region particle–bed interaction has little direct influence on the dynamics of the flow.

In the upper regions of the flow particle settling results in portions of the flow becoming more buoyant than the ambient atmosphere as the interstitial fluid is less dense than the ambient fluid (Fig. 5). Likewise shear instabilities (Kelvin–Helmholtz) are promoted as density gradients between the flow and the ambient atmosphere decrease, resulting in smaller Richardson numbers (Fig. 6). Both plumes and shear instabilities

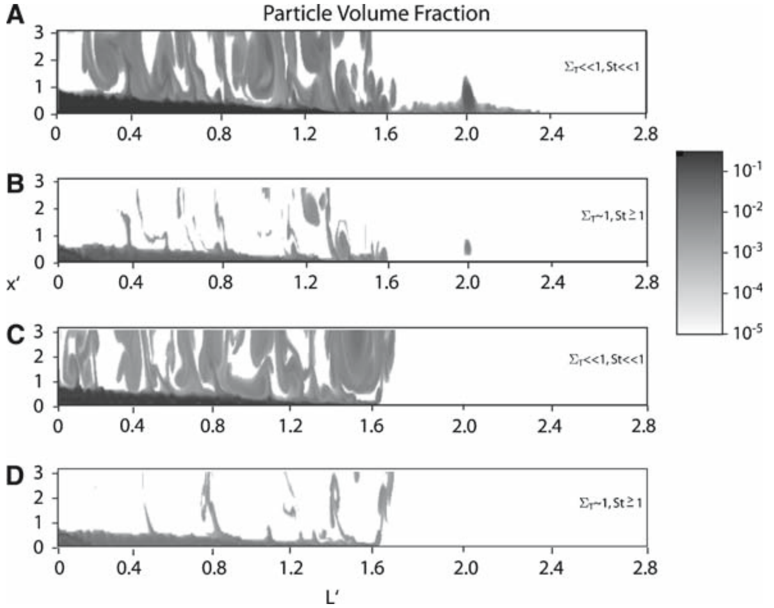

Fig. 5 Particle volume fraction for the binary particle mixtures with saltating (**a, b**) and leaky (**c, d**) boundaries for flow condition 1 (Table 2). **a** and **c** show the small stability factor particles, and **b** and **d** show the large stability factor particles. This figure represents the instantaneous particle volume fraction at $t' = 4$. The leaky boundary flow has reached its maximum run-out and at $L' \sim 1.6$ where the flow becomes more buoyant than the ambient fluid. The saltating boundary condition flow continues to propagate to the right with a greater amount of large stability factor particles than the leaky boundary counterpart. Shear and buoyancy instabilities generate the eddies that rise above $H' = 1$ in these flows

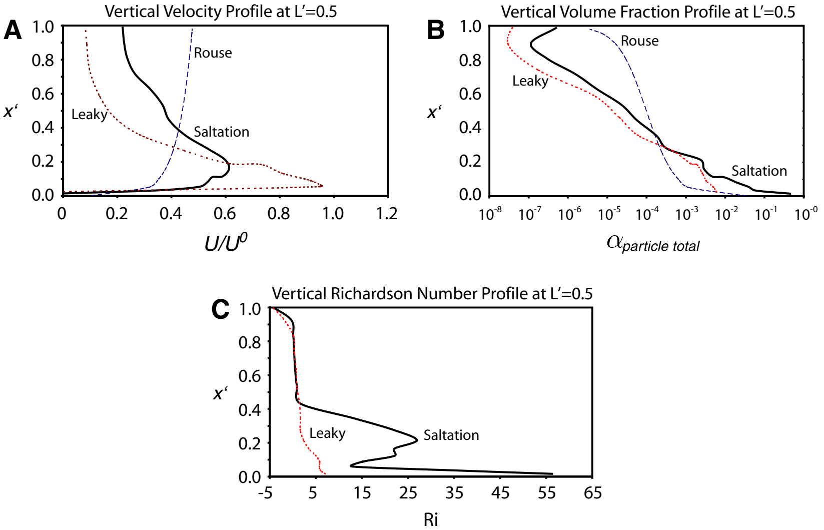

Fig. 6 Vertical profiles of flow condition 1 at $L' = 0.5$. **a** The vertical velocity for leaky (*small dashed line*) is compared to the saltation (*solid black line*) and a Roussean profile (*large dashed line*). The Roussean profile is discussed in Sect. 6 **b** The vertical volume fraction profile of the saltation, leaky and Roussean profile is shown. The *base* of the saltation curve shows order of magnitude greater volume fraction in the region of bed-load transport

preferentially remove the fine-grain, small-stability-factor particles from the flows (Fig. 5). The larger grain sizes ($\Sigma_T \sim 1$) that do rise above the scale height of the flow are typically confined to the core of the plumes where the vertical velocity is the greatest or are centrifuged to the edge of the Kelvin–Helmholtz eddies. However, the average volume fraction of particles above the neutral buoyancy height of the flow is less than 10^{-4} and the total volume fraction of particles above the scale height remains below 5% of the total flow.

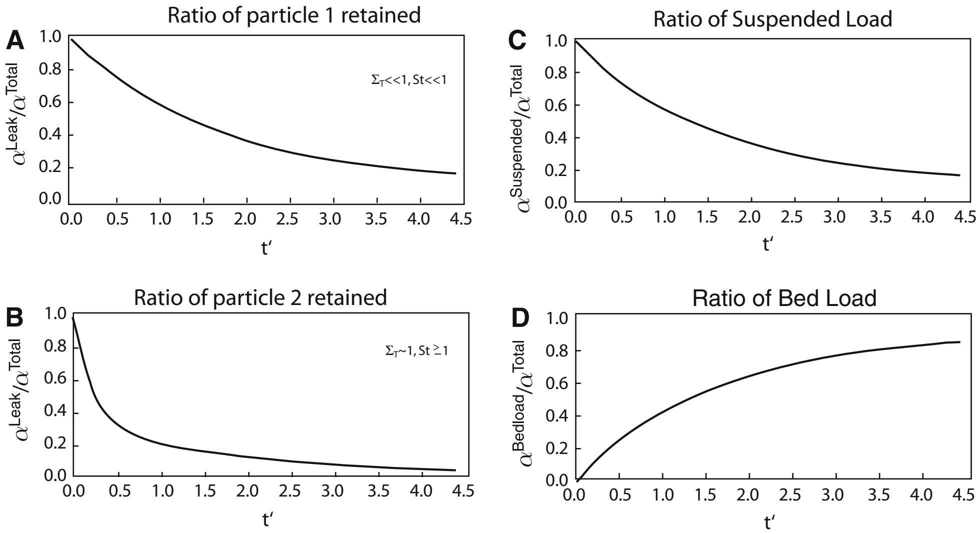

Fig. 7 Rate of particle loss and rate of development of bed-load and suspended load for flow conditions 1. **a** and **b** give the rate of loss of particle 1 (small-stability-factor particles) and particle 2 (large-stability-factor particles), respectively. The rate of loss of the small-stability-factor particles is close to exponential whereas the rate of loss of the large-stability-factor particles shows a distinct inflection near $t' = 0.5$. **c** and **d** show the ratio of suspended and bed-load in the saltating boundary flows. Similar to the loss of small-stability-factor particles, the volume of material in the bed-load grows exponentially with time

5.2 Dynamics and evolution of bed-load

Although the flows are similar above ∼10% the scale height of the flow, the boundary conditions provide the template for the transport capacity and energy of the bed-load region of the flow. As particles migrate to the base of the flow they are either sedimented through the leaky interface (simulations $1L$–$4L$) or begin interacting through saltation (simulations $1S$–$4S$). When considering the saltation boundary at $L' = 1$, the temporally averaged bed-load comprises 40–50% of the total load of the flow, and the majority of the energy of the flow. However, the volume of particles in the bed-load increases with time as particles settle from the suspended load. For example after $t' = 4$ greater than 80% of the volume of particles is in the bed-load (Fig. 7).

The rate at which particles enter the bed-load region of the flow is proportional to the settling velocity of the particles. The transfer rate of the small stability factor particles is close to exponential (Fig. 7), and since these particles represent 95% of the original volume fraction of the particles, the growth of the bed-load layer is also exponential. However, the ($\Sigma_{\mathrm{T}} \sim 1,\ St \geq 1$) particles have a distinct inflection in the rate at which they are transferred to the bed (Fig. 7). Spatially, the $\Sigma_T \sim 1$ particles are transferred from the suspended load into the bed-load primarily from 0 to $0.5L'$ regardless of the initial velocity of the gravity current. In contrast, the ($\Sigma_T \ll 1,\ St \ll 1$) particles are transferred to the bed over a much wider area and are more sensitive to the initial conditions of the flow (Fig. 8). For instance, the small-stability-factor (Table 2) particles remain in suspension more efficiently for the high-Reynolds-number flows and sediment over a greater distance.

5.3 Vertical and lateral particle size sorting in transient flows

The greater sedimentation rate of the $\Sigma_T \sim 1$ particles leads to a much greater proportion of the small stability factor particles remaining in the flow for leaky boundary conditions. We compare sorting in these flows normalized to their initial proportions:

$$\gamma' = \frac{{}^2\alpha/{}^1\alpha}{{}^2\alpha^0/{}^1\alpha^0}. \tag{44}$$

The sorting coefficient (γ') is greater than one if enriched in the larger grain size relative to the initial proportion and less than one if a greater amount of fine particles are present. In the negative log plots of Figs. 9 and 10, positive values correspond to an enrichment of fine material and negative values correspond to an enrichment of the coarse material. For leaky flow boundary conditions the sorting coefficient is almost always

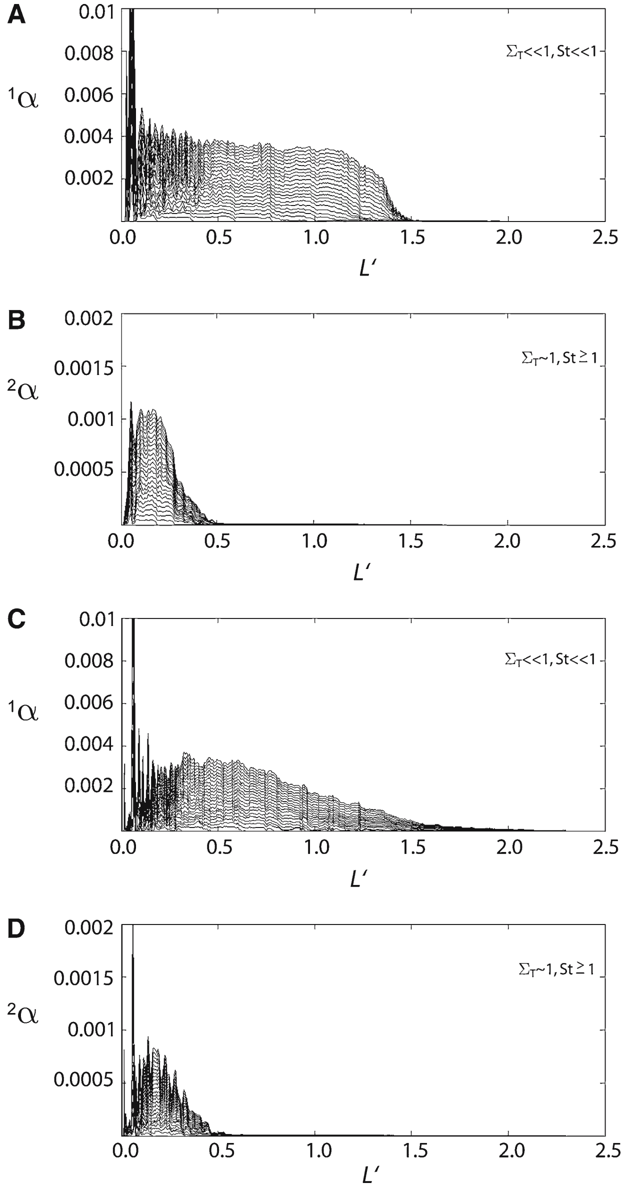

Fig. 8 The progressive loss of particles for flow conditions 2 and 4. The individual lines represent the cumulative loss of material at different times (in $t' = 0.15$ intervals). **a** and **b** apply to flow conditions 2 and **c** and **d** refer to the more energetic flow conditions 4. Particle loss is normalized by the total volume of particles introduced in the flow. In panel **A** the small-stability-factor particles leak through the basal boundary from 0 to 1.6 at which point the flow becomes more buoyant than its surroundings. Panel **b** shows the particle loss of the large stability factor particles which are mostly confined to less than $L' = 0.5$. For the more energetic inlet conditions the small stability factor particles **c** are distributed over a much wider area, but again the large stability factor particles **D** are mostly confined to less than $L' = 0.5$

less than 1, and on average the flow becomes progressively depleted in the large grain size with distance from the inlet. However, there is significant structure to the sorting of particles at single instant in time (Fig. 9). The head of the current typically has regions where the sorting coefficient approaches (but rarely exceeds) unity for the leaky boundary flows.

In contrast, the bed-load region of the flow that develops in the saltation simulations has a sorting coefficient much greater than unity initially, becoming progressively more mixed with time due to the accumulation of small-stability-factor particles. The front of the these flows are also enriched in the large-stability-factor component and is one of the few locations that has sorting coefficients greater than unity (Fig. 10). This effect can be explained by the relative phase velocities of the two particle species. Strong vortices develop near the front

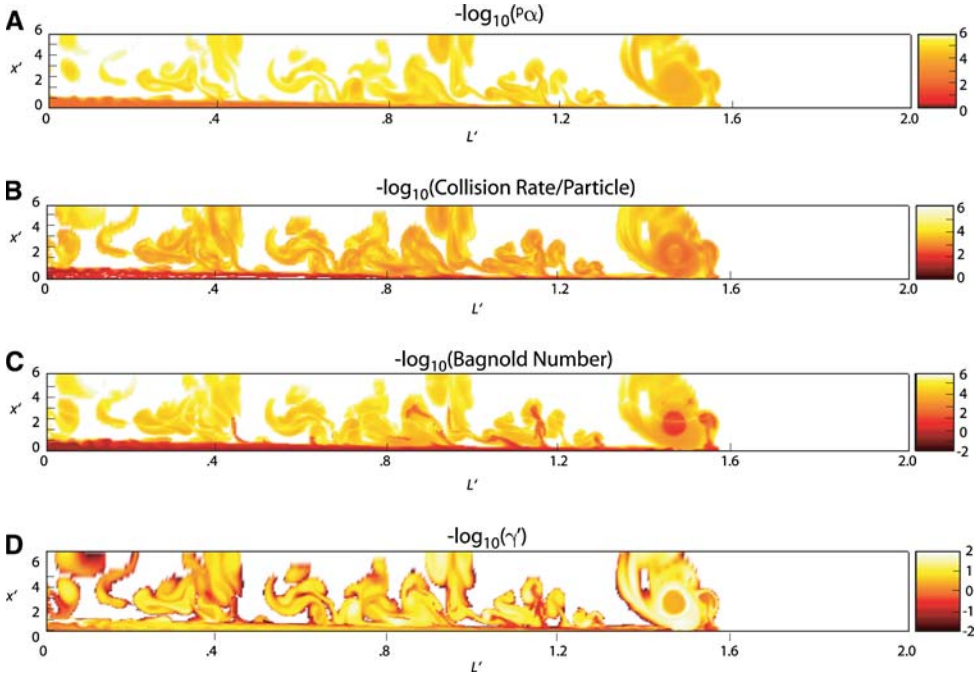

Fig. 9 Flow traversing leaky boundary (flow conditions 1) and $t' = 3$. **a** The $-\log 10$ of the particle volume fraction, **b** $-\log 10$ of the collision rate/particle, **c** $-\log 10$ of the Bagnold number, **d** $-\log 10$ of the sorting coefficient (positive values indicate enrichment of fine particles, negative values indicate enrichment of coarse material relative to the inlet values. Except near the inlet, the sorting coefficient remains positive (fine enriched) although portions of the head of the flow have near-zero values

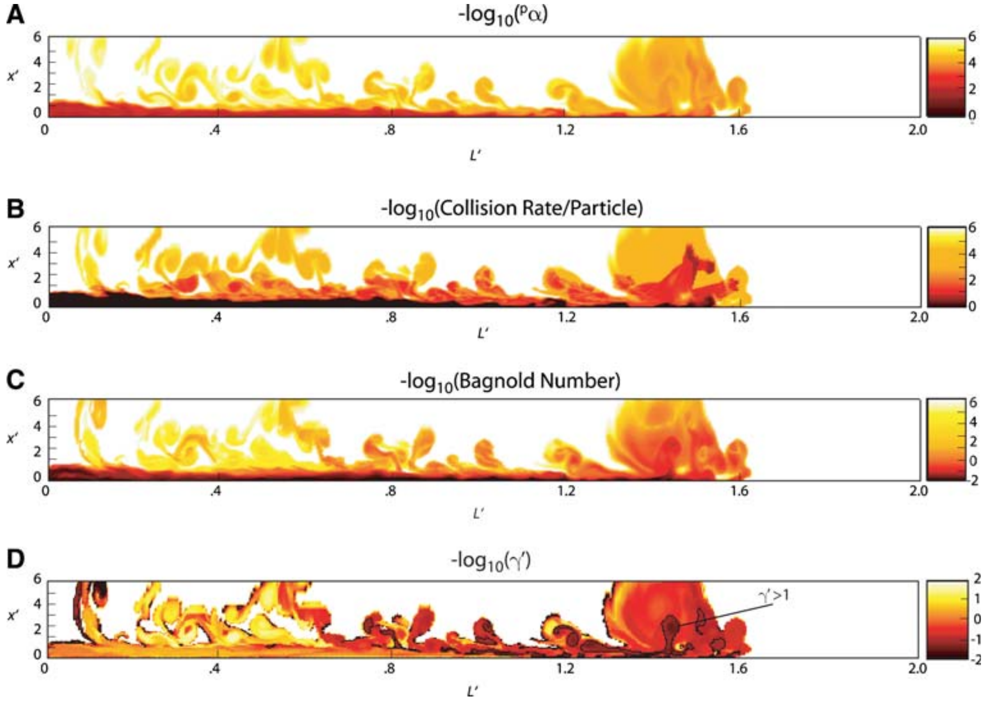

Fig. 10 Flow traversing saltating boundary (flow conditions 1) and $t' = 3$. **a** The $-\log 10$ of the particle volume fraction, **b** $-\log 10$ of the collision rate/particle, **c** $-\log 10$ of the Bagnold number, **d** $-\log 10$ of the sorting coefficient (positive values indicate enrichment of fine particles, negative values indicate enrichment of coarse material relative to the inlet values). Fig. 9 shows that for the same inlet flow conditions the volume fraction and collision rate are much greater at the base of the saltating flows compared to the leaky boundary flows (Fig. 8). The saltating flows are also more efficient at transporting the large-stability-factor particles (**d**) and near the front of the flow there are even regions where there is an enrichment of course material relative to inlet conditions (*outlined in black*)

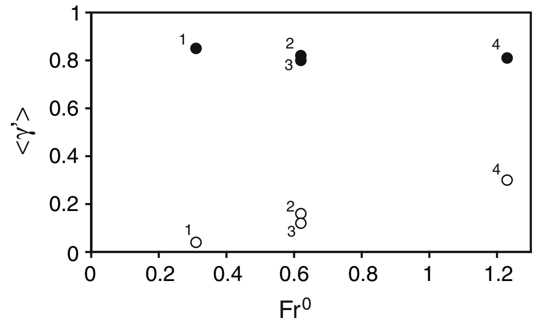

Fig. 11 The vertically and temporally averaged sorting coefficient at $L' = 0.5$ for flow conditions 1–4 and saltating (*dark circles*) and leaky (*open circles*) boundary conditions. The *numbers to the right of the circles* indicate the inlet conditions (Table 2). The sorting coefficients are plotted relative to their inlet Froude numbers. The leaky boundary sorting coefficient is sensitive to the inlet Froude number, whereas the inlet flow energy has little influence on the sorting coefficient for the saltating boundary flows

of the flow exert drag on the particles. This non-steady forcing influences the small-stability-factor particles to a greater degree than the larger-stability-factor particles, and hence the larger grain sizes have a tendency to accumulate at the front of the granular flows. Likewise, the elutriation rate of fine particles in buoyant plumes is much greater than the large particles and so dilution near the top of the current head will preferentially remove the fine component. In the leaky flows the elutriation rate is outpaced by sedimentation through the basal boundary (Fig. 8). However for saltation boundary conditions the energetic front of the flow has sufficient shear that little of the material is deposited and hence the only major particle sink from the current head is elutriation which preferentially removes fine particles.

The vertically and temporally averaged sorting coefficient $< \gamma' >$ at $L' = 1$ for the different flows is shown in Fig. 11 as a function of the densimetric Froude number. In general the sorting coefficient is higher for the saltation boundaries than for leaky boundary flows. The fundamental differences in the sorting behavior between flows that have leaky or saltation boundaries is due to the longer residence time of particles in the saltation flows. In saltating flows, particles will have multiple encounters with the base and can be remobilized due to shear and particle collisions after encountering the base of the flows. This is modeled as a partial slip velocity (Fig. 6). As larger particles can remain mobilized in the flow due to saltation, the downstream volume fraction is less diminished relative to leaky boundary flows. For the leaky flows the mean particle sorting at $L' = 1$ is largest for the highest initial kinetic energy. Vertically averaged sorting in saltation flows is much less sensitive to their initial kinetic energy, although Figs. 9 and 10 demonstrate that they are much more heterogeneous in particle sorting vertically and laterally compared to leaky flows.

5.4 The influence of bed interaction on run-out distance

The run-out distance and mean residence time of particles in a flow is controlled by the complex interplay of flow dilution and buoyancy and energy dissipation due to particle–particle and particle-boundary interactions. For the leaky boundary flows, the run-out distance is ultimately a result of flow dilution and buoyancy reversal. While suspension and entrainment mechanism also operate in saltation boundary flows, inelastic collisions in the bed-load determines the maximum run-out of the ground-hugging portion of the flow. Although inelastic collisions and dilution due to particle loss are distinct physical mechanisms, they can both be described by energy dissipation relative to the total kinetic energy budget of the flow. In the case of leaky boundary conditions kinetic energy is removed from the flow due to mass loss (i.e., particles settling through the leaky boundary are removed from the flow). However, particles that reach the boundary in saltation flows lose only a portion of their energy for every particle–wall interaction. While it is true that after the particles have reached the base of the saltation flows they dissipate energy due to inelastic collisions with other particles and the wall, the rate at which this occurs is necessarily slower than if all energy from a particle is lost the instant it touches the bottom boundary as in the case of the leaky boundary. Particle-boundary energy dissipation was greater than any other mechanism. Over a fluid timescale, the leaky boundary dissipates kinetic energy more efficiently than saltation and this correlates well with run-out distance (Fig. 12).

For both flow conditions 1 and 2, the maximum run-out distance is greater for the saltation boundary flows than for the leaky boundary flows. Similarly, the residence time of an average particle is much longer for all

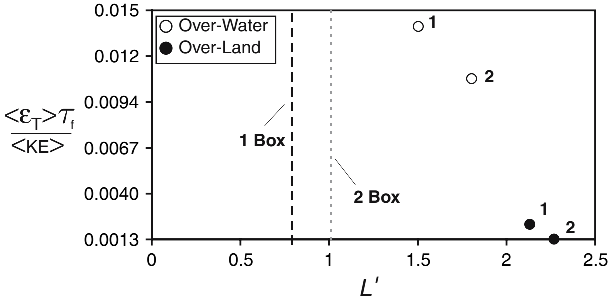

Fig. 12 The dissipation of kinetic energy during a fluid timescale versus run-out distance for flow conditions 1 and 2. Dissipation rate is normalized by the total kinetic energy of the flow and the timescale of fluid motion. Again inlet conditions are indicated by the *number near the circles* and *dark circles* represent saltation boundaries. Box models using the same inlet conditions are plotted for comparison (although dissipation rate at boundary does not apply for these calculations). For both flow conditions 1 and 2 the run-out distance is greater for saltating flows than for leaky boundary flows

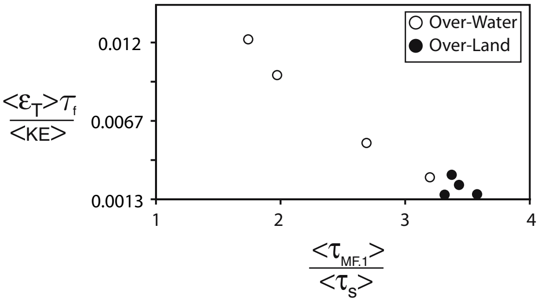

Fig. 13 The dissipation of kinetic energy during a fluid timescale at the boundary versus the residence time (until 10% of the volume remains). The dissipation rate is normalized by the total kinetic energy and fluid timescale, and the 10% residence time is normalized by the settling velocity of small stability factor particles. The residence time of particles correlates with diminished dissipation rate. Particles in the saltating boundary flows have a greater residence time than their leaky flow counterparts, but the residence time in the saltating flows is relatively insensitive to the inlet conditions explored

four flow conditions if saltation boundary flows are considered, although the differences are minimized for flows with the greatest initial kinetic energy (Fig. 6). One measure of this is to examine the mean residence time of particles until the flow has decayed to 10% its initial volume flux normalized relative to the settling timescale of an average particle. As the flows become more dilute (or have lower inlet energy) this measure of residence time approaches unity for the suspended load (Fig. 13). As both Reynolds number and concentration increase the suspended load portion of the flow has a greater residence time due to turbulent suspension and to particle–particle collisions.

6 Discussion

6.1 Dominant modes of momentum transfer

The development of bed-load in particle-laden flows alters the primary mechanism of momentum transfer from particle-fluid drag to particle–particle collisions. This is depicted in Figs. 9 and 10 where, for $x' < 1$, the collision rate per particle is over an order of magnitude greater in the saltation boundary conditions. A conventional measure of the collisional redistribution of momentum relative to particle–fluid drag is given by the Bagnold number:

$$N_{\mathrm{Bag}} = \frac{{}^{p}\alpha \rho_{\mathrm{s}} D^2 \eta}{(1 - {}^{p}\alpha)\mu}, \tag{45}$$

where η is the strain rate and μ is the viscosity of the interstitial fluid. Based on empirical observations, Iverson [44] suggested that flows with Bagnold numbers greater than ~ 200 would have a greater momentum transfer due to particle collisions rather than particle–fluid drag. Although this transition is not rigorously defined, the saltation boundary flows clearly have regions of the flow with a Bagnold number greater than 200, whereas the densest portions of the leaky boundary flows are less than $N_{\mathrm{Bag}} = 200$ (Figs. 9c, 10c).

One of the primary ways that the development of bed-load, and the resulting increase in particle–particle collisions, manifests itself is in the mixing of different particle species. In the suspended-load portion of a flow, particles of different size and density, and hence with different stability factors and Stokes numbers, will be become segregated relative to each other. This is particularly relevant in situations similar to these simulations where the stability factor is much less than 1 in the case of the smallest particles and near to unity for the largest particles. As shown in Fig. 5 the large-stability-factor particles are confined to the lower portions of the flow, and are nearly absent in the formation of mesoscale structures due to the development of shear and buoyancy instabilities. Hence, the leaky boundary flows that have only suspended-load transport are efficient at unmixing different grain sizes and producing sorting that reflects energy of the flow (Fig. 11). For instance, lower inlet Froude numbers produced smaller sorting coefficients (more poorly sorted) at the flow scale length ($L' = 1$) for leaky boundary flows (Fig. 11).

In contrast, the inlet kinetic energy (and inlet Froude number) and sorting number at $L' = 1$ are poorly correlated for saltating flows (Fig. 11). Particle–particle collisions and particle–boundary collisions can keep multiple grain sizes mobile, mixing particles with different stability factors. This result is consistent with the observation that in channel flow particle–wall and particle–particle collisions have a tendency to flatten the particle concentration across the channel [45,46]. Once particles enter the bed-load region they are homogenized by the increased number of particle collisions, and mesoscale structure and fluctuations initially present in the suspended portion of the flow are subdued. The bed-load mixing mechanism likely plays a role in the development of massive, homogenous pyroclastic flow deposits. Changes in vertical grading in flows that have developed bed-load transport reflect the integrated upstream mean particle supply to the bed-load region, rather than local mesoscale turbulent structure of the flow.

6.2 The role of particle stratification compared to homogeneous flows

Particle-laden flows are manifestly heterogeneous in particle volume fraction and particle size sorting. A comparison between these simulated flows which track these heterogeneities and simplified approaches yields further insight in the relative importance of particle volume fraction heterogeneity on flow transport. Two common approaches to the treatment of particle-laden gravity currents is to either assume homogeneity in particle volume fraction within the current or to assume particle volume fraction gradients based upon the advection–diffusion of sediment (i.e., the Rouse approach).

For homogeneous transport, one approach to the prediction of the evolution of the current is to assume constant volume (no entrainment) and a front condition (usually $Fr_{\mathrm{d}} \sim 1$). This approach is sometimes called the box-model approach due to the box-shaped profiles produced with these assumptions [47,48]. Using a box-model approach, a run-out distance can be predicted at the point at which enough particles have sedimented to generate a buoyancy reversal. Key assumptions in this approach are that sedimentation rate is given by the settling velocity, once removed from the flow particles cannot become resuspended, and there is no cooling or entrainment (both of which would lower the interstitial gas density). Modifying the approach of Dade and Huppert [47] to a 2D current gives the following relation for current length:

$$R = \frac{-\ln\left({}^{p}\alpha / {}^{p}\alpha^{0}\right)\dot{q}}{w_{\mathrm{s}}}, \tag{46}$$

where $\dot{q}$ is the constant volume flux $(u \cdot h)$. When the mixture density equals the ambient fluid density $\sum_{\mathrm{p}} \rho_{\mathrm{p}}\alpha_{\mathrm{p}} + \rho_{int}\alpha_{g} = \rho_{\mathrm{amb}}$, the current will begin to ascend.

Run-out distances using the box-model approach were shorter than predicted in the simulations (Fig. 12) compared to either the saltating boundary flows or the leaky boundary flows. The assumptions used in developing the box-model approach emphasize suspended load conditions. For instance, the $Fr_{d} \sim 1$ front condition most clearly matches the results of the leaky boundary, suspended load flows. In contrast, the densimetric Froude number deviates significantly from unity when an interacting bed-load develops. The differences in run-out distance between the leaky boundary flows and the box-model approach can principally be attributed to cooling and entrainment, increasing the average gas density in the simulations. Hence neutral buoyancy is reached for a much more particle-dilute flow which gives the flow a greater period of time to propagate. For example, the mean temperature below the scale height is 412 K at the maximum run-out distance for flow conditions 1 and leaky boundary conditions. The mean volume fraction below the scale height at this location is 1.6×10^{-4}. In contrast, without cooling or entrainment the interstitial gas density remains constant and the particle volume fraction at neutral buoyancy is 3.3×10^{-4}, or nearly 200% greater particle volume fraction than when considering entrainment. Hence, if the interstitial fluid is less dense than the ambient fluid, the run-out distance will be linked closely with entrainment efficiency. (In this case the box model is a proxy for completely inefficient mixing.) Particle sedimentation decreases the Richardson number (Fig. 6) and lowers the required shear for efficient entrainment, and incorporating this effect will lead to run-out predictions of over a factor of 200% different if vertical mixing does not occur.

Particle stratification models based upon mixing-length approximations to turbulent flow have been proposed in a number of settings [49–51]. Using an eddy diffusivity proportional to the scale height of the flow (and assuming unidirectional, open-channel flow at equilibrium) yields a Roussean particle volume fraction profile:

$$^{p}\alpha = \alpha_b \left(\frac{(H - H')/H'}{(H - b)/b} \right)^{Pn}, \tag{47}$$

where b is reference height near the base of the flow, α_b is the particle volume fraction at b, and Pn is the Rouse number ($Pn = \frac{w_s}{\kappa u_*}$, where w_s is the settling velocity, $u_*$is the shear velocity, and κ is the von Karman constant). Valentine [51] applied this concept to pyroclastic flow transport, and predicted vertical gradients in the particle volume fraction. The Roussean particle volume fraction profile and open-channel velocity profiles using average shear velocity are compared to the volume fraction and velocity profile of these simulations at $L_{0.5}$ (Fig. 6). As expected, the particle volume fraction in the Roussean profiles deviates significantly compared to the bed-load region of the saltation simulations due to the equilibrium assumption of balanced vertical particle flux inherent in the Roussean derivation. The vertical particle volume fraction gradients in the Roussean profile are also considerably smaller than leaky boundary condition simulations. The shear instabilities and entrainment at low Richardson numbers at the top of these currents helps to explain the differences between an equilibrium Roussean profile and the leaky gravity currents. The open-channel assumption of the velocity profile for the Roussean derivation predicts maximum velocity at the top of the current, whereas the simulations predict maximum velocities at approximately 1/3 the current scale height, similar to experimental gravity currents [52].

6.3 Development of bed-load and implications for changing boundary conditions

Bed-load material is continuously supplied from the suspended-load region, which suggests that this layer can reform after changes in boundary conditions (i.e., from leaky to saltation boundaries). As an example, using inlet conditions 1 (Table 3) a simulation was conducted with leaky boundaries to L'=1 and saltating boundaries thereafter. By $L' = 1.1$ scale length units a particle-rich bed-load region had developed after crossing the transition for leaky to saltating boundaries. This bed-load region was characterized by increased particle–particle collisions relative to its completely leaky flow counterpart and Bagnold numbers in excess of 1,000. However, as most of the large-stability-factor particles had been removed during transit over the leaky boundary condition, the vertically averaged sorting coefficient of this bed-load region was ~ 0.04 at $L' = 1.1$ and much less than a completely saltating boundary (Fig. 10). These simulations provide an important caveat in the interpretation of well-sorted deposits; they can imply particle capture upstream of deposition rather than locally dilute, suspended load conditions. Besides the transition from leaky to saltating boundaries, changes in topography may also alter the transition from suspended load to bed-load in particle-laden gravity currents if the bed-load is removed after encountering particularly steep landscapes [10,51,53,54]. Understanding the removal and formation of bed-load determines the amount of force that these currents supply to the near-bed region and determines how hazardous a given flow will be to near-bed structures and populations.

7 Conclusions

The formation of bed-load transport in ground-hugging particle-laden flows is a natural consequence of particle–bed interaction. The proportion of bed-load material is continuously evolving as particles that can no longer be suspended are transferred to the basal region of the flow. Saltation due to inelastic collisions at the bed results in increased particle volume fractions near the bed and a greater number of particle–particle collisions. These collisions homogenize the concentration of different size particles and can result in greater residence time of particles in the flow. Entrainment and particle–fluid drag are capable of resuspending some material from the bed-load at the front of the current, and the preferential removal of fine material leaves portions of the bed-load at the front of the flow enriched in coarse material. The increased mobility of particles at the base of the flow also results in greater run-out distance of these flows relative to completely leaky conditions by as much as 25%.

When flows encounter a leaky boundary (such as traversing water) bed-load formation is inhibited and a more dilute suspended-load transport develops. Particles are organized into mesoscale structures due to particle–fluid interaction, and particles with different Stokes numbers are readily sorted relative to each other. The dilution in particle volume fraction that develops at the upper interface of these flows encourages shear instabilities and buoyancy reversal, and this results in entrainment of ambient fluid in the flow. Ultimately these flows become so dilute that they can no longer propagate as ground-hugging currents. Hence, the dichotomy of dense, bed-load transport and completely suspended load transport can be explained by particle–bed interaction and this interaction is one of the principle factors determining run-out length and order–disorder in deposits.

Acknowledgements We thank two anonymous reviewers and the editor, Prof. H.J.S. Fernando, for their comments and suggestions, which have helped improve this manuscript. This work was supported by a NASA Earth Systems Science Fellowship (JD) and a National Science Foundation grant, EAR-0440391 (GB).

Appendix

Momentum equation constitutive relations

- Stress tensor

$$^{m}\tau_{ij} = 2\,^{m}\alpha\,^{m}\mu\,^{m}e_{ij} + {}^{m}\alpha\left(^{m}\lambda - \frac{2}{3}\,^{m}\mu\right)\frac{\partial\,^{m}U_i}{\partial x_i}\delta_{ij}, \tag{A1}$$

- Rate of strain

$$^{m}e_{ij} = \frac{1}{2}\left(\frac{\partial\,^{m}U_i}{\partial x_j} + \frac{\partial\,^{m}U_j}{\partial x_i}\right). \tag{A2}$$

Granular phases

- Total granular pressure

$$^{p}P = {}^{p}P^{\mathrm{f}} + {}^{p}P^{k/c} \tag{A3}$$

- Total bulk viscosity

$$^{p}\lambda = {}^{p}\lambda^{\mathrm{f}} + {}^{p}\lambda^{k/c} \tag{A4}$$

- Total shear viscosity

$$^{p}\mu = {}^{p}\mu^{\mathrm{f}} + {}^{p}\mu^{k/c} \tag{A5}$$

- Kinetic–collisional pressure

$$^{p}P^{k/c} = {}^{p}\alpha\,^{p}\rho\,^{p}\theta\left[1 + 2\,^{p}\alpha g_0(1+e)\right] \tag{A6}$$

- Total kinetic–collisional viscosity

$$^{p}\mu^{k/c} = {}^{p}\alpha\,^{p}\rho\left(^{p}\nu^{\mathrm{kin}} + {}^{p}\nu^{\mathrm{coll}}\right) \tag{A7}$$

- Kinetic shear viscosity

$$^{p}\nu^{\mathrm{kin}} = \left[\frac{2}{3}k_{12}\eta_t + {}^{p}\theta(1 + \zeta_{c2}\,^{p}\alpha g_0)\right]\tau_p \tag{A8}$$

- Collisional shear viscosity

$$ {}^{p}\nu^{\mathrm{coll}} = \frac{8}{5}{}^{p}\alpha g_0 \frac{(1+e)}{2}\left({}^{p}\nu^{kin} + d\sqrt{\frac{{}^{p}\theta}{\pi}}\right) \tag{A9} $$

- Collisional bulk viscosity

$$ {}^{p}\lambda = \frac{5}{3}{}^{p}\alpha^{p}\rho^{p}\nu^{coll} \tag{A10} $$

- Frictional pressure

$$ P^{\mathrm{f}} = a_{fs}\frac{({}^{1}\alpha^{\max} - {}^{1}\alpha)^{b_{\mathrm{fs}}}}{({}^{1}\alpha - {}^{1}\alpha^{\min})^{b_{\mathrm{fs}}}}, \quad \text{for } {}^{1}\alpha^{\min} < {}^{1}\alpha < {}^{1}\alpha^{\max}, \ \text{ else } P^{\mathrm{f}} = 0 \tag{A11} $$

- Effective viscosity frictional regime

$$ {}^{p}\mu^{\mathrm{f}} = \frac{P^{\mathrm{f}} sin^{2\,p}\phi}{\sqrt{4\sin^{2}{}^{p}\phi\,{}^{p}I_{2\mathrm{D}} + \left(\frac{\partial^{p}U_i}{\partial x_i}\right)^{2}}} \tag{A12} $$

- Bulk viscosity frictional regime

$$ {}^{p}\lambda^{\mathrm{f}} = -\frac{2}{3}{}^{p}\mu^{\mathrm{f}} \tag{A13} $$

Fluid phase
- Total shear viscosity

$$ {}^{1}\mu = {}^{1}\mu^{\mathrm{mol}} + {}^{1}\mu^{t} \tag{A14} $$

- Molecular viscosity

$$ {}^{1}\mu^{\mathrm{mol}} = 1.7 \times 10^{-5}\left(\frac{{}^{1}T}{273}\right)^{1.5\left(\frac{383}{{}^{1}T+110}\right)} \tag{A15} $$

- Effective turbulent viscosity

$$ {}^{1}\mu^{t} = {}^{1}\rho C_{\mu}\frac{\left({}^{1}k\right)^{2}}{{}^{1}\varepsilon} \tag{A16} $$

- Bulk viscosity

$$ {}^{1}\lambda = -\frac{2}{3}\left({}^{1}\mu\right) \tag{A17} $$

- Particle–gas drag

$$ {}^{1}I_i = \beta\left({}^{1}U_i - {}^{p}U_i\right) - {}^{p}\alpha\frac{\partial}{\partial x_i}{}^{1}P \tag{A18} $$

where

$$ \beta = \frac{3^{p}\alpha^{1}\alpha^{1}\rho}{4V_r d}C_D^{s}\left|{}^{1}U_i - {}^{p}U_i\right| \tag{A19} $$

- Ratio of terminal velocity of a group of particles to the single-particle terminal velocity

$$V_{\mathrm{r}} = 0.5(A - 0.06Re_{\mathrm{p}} + \sqrt{(0.06Re_{\mathrm{p}})^2 + 0.12Re_{\mathrm{p}}(2B - A) + A^2} \tag{A20}$$

where

$$A = {}^1\alpha^{4.14} \tag{A21}$$

$$B = \begin{cases} 0.8\,{}^1\alpha^{1.28} & \text{if } {}^1\alpha \leq 0.85 \\ {}^1\alpha^{2.65} & \text{if } {}^1\alpha > 0.85 \end{cases} \tag{A22}$$

- Drag coefficient

$$C_{\mathrm{D}}^{s} = \left[0.63 + \frac{4.8}{\sqrt{Re_p}}\right]^2 \tag{A23}$$

- Particle Reynolds number

$$Re_{\mathrm{p}} = \frac{d\left|{}^pU_i - {}^1U_i\right|{}^1\rho}{{}^1\mu} \tag{A24}$$

- Momentum transfer between particle phases

$${}^pI_i = -F_{\mathrm{sp}}({}^pU_i - {}^sU_i), \quad s \neq p \tag{A25}$$

- Coefficient of interphase force between particle phases

$$F_{\mathrm{sp}} = \frac{3(1+e)\left(\frac{\pi}{2} + F_c\frac{\pi^2}{8}\right)\left({}^2\alpha\right)\left({}^2\rho\right)\left({}^3\alpha\right)\left({}^3\rho\right)({}^2d + {}^3d)^2 g_0({}^2U_i - {}^3U_i)}{2\pi\left(\left({}^2\rho\right)\left({}^2d\right)^3 + \left({}^3\rho\right)\left({}^3d\right)^3\right)} + H_1 P^{\mathrm{f}} \tag{A26}$$

- Radial distribution function

$$g_0 = \frac{1}{{}^0\alpha} + \frac{3\left({}^1d\right)\left({}^2d\right)}{\left({}^0\alpha\right)^2\left({}^1d + {}^2d\right)}\left[\frac{{}^1\alpha}{{}^1d} + \frac{{}^2\alpha}{{}^2d}\right] \tag{A27}$$

Turbulence and pseudo-thermal energy closure equations

- Granular energy conductivity

$${}^p\kappa = {}^p\alpha\,{}^p\rho({}^p\kappa^{\mathrm{kin}} + {}^p\kappa^{\mathrm{coll}}) \tag{A28}$$

- Kinetic component of granular energy conductivity

$${}^p\kappa^{\mathrm{kin}} = \left(\frac{9}{10}k_{12}\eta_t + \frac{3}{2}{}^p\theta(1 + v_c\left({}^p\alpha\right)g_0)\right)\left(\frac{9}{5t_{12}^{x}} + \frac{\xi_c}{{}^pt^c}\right)^{-1} \tag{A29}$$

- Collisional component of granular energy conductivity

$${}^p\kappa^{coll} = \frac{18}{5}\left({}^p\alpha\right)g_0\frac{(1+e)}{2}\left({}^p\kappa^{kin} + \frac{5}{9}\left({}^pd\right)\sqrt{\frac{{}^p\theta}{\pi}}\right) \tag{A30}$$

- Dissipation of particle fluctuating energy

$${}^p\varepsilon = 12(1 - e^2)\left({}^p\alpha\right)^2\left({}^p\rho\right)g_0\frac{{}^p\theta^{3/2}}{{}^pd} \tag{A31}$$

- Turbulence exchange terms

$$\Pi_{k1} = \beta\left(k_{12} - 2\left({}^1k\right)\right) \tag{A32}$$

$$\Pi_{\varepsilon 1} = C_{3\varepsilon}\left(\frac{{}^1\varepsilon}{{}^1k}\right)\Pi_{k1} \tag{A33}$$

$$\Pi_{k2} = \beta(k_{12} - 3\left({}^p\theta\right)) \tag{A34}$$

$$k_{12} = \frac{\eta_t}{1 + (1 + X_{p1})\eta_t}(2\left({}^pk\right) + 3X_{21}{}^p\theta) \tag{A35}$$

- Particle relaxation timescale

$$t_{12}^x = \frac{{}^p\alpha{}^p\rho}{\beta} \tag{A36}$$

- Energetic eddies times scales

$${}^1t^t = \frac{3}{2}C_\mu\frac{{}^1k}{{}^1\varepsilon} \tag{A37}$$

- Fluid Lagrangian integral time scale

$$t_{12}^t = \frac{t_1^t}{\sqrt{1 + C_\beta\xi_r^2}} \tag{A38}$$

- where

$$\xi_r^{\mathrm{p}} = \frac{3|U_r|^2}{2\left({}^1k\right)} \tag{A39}$$

$$C_\beta = 1.8 - 1.35cos^2(\theta) \tag{A40}$$

- Collisional time scale

$${}^pt^c = \frac{{}^pd}{6({}^p\alpha)g_0\sqrt{16{}^p\theta/\pi}} \tag{A41}$$

$$\frac{1}{{}^pt} = \frac{2}{t_{12}^x} + \frac{\sigma_c}{{}^pt^c} \tag{A42}$$

- Collisional constants

$$\zeta_{c2} = 7\frac{2}{5}(1 + e)(3e - 1) \tag{A43}$$

$$\upsilon_c = (1 + e)^2(2e - 1)/100 \tag{A44}$$

$$\zeta_c = (1 + e)(49 - 33e)/100 \tag{A45}$$

$$\sigma_c = (1 + e)(3 - e)/5 \tag{A46}$$

$$X_{p1} = \frac{{}^p\alpha{}^p\rho}{{}^1\alpha{}^1\rho} \tag{A47}$$

Thermal energy constitutive relations

- Thermal conductivity

$${}^m_{\mathrm{Th}}k = {}^mk^{eff} + {}^mk^t \tag{A48}$$

- Effective conductivity of the gas phase

$${}^1k^{\mathrm{eff}} = (1 - \sqrt{1 - {}^1\alpha})\left(0.025\sqrt{\frac{{}^1T}{300}}\right) \tag{A49}$$

- Turbulent conductivity of gas phase

$$ {}^{1}k^{t} = \frac{\left({}^{1}\alpha\right)\left({}^{1}c_{p}\right)\left({}^{1}\mu^{t}\right)}{Pr} \tag{A50}$$

- Effective conductivity of the particle phases

$$ {}^{p}k^{\mathrm{eff}} = {}^{1}_{\mathrm{Th}}k\left[\frac{\phi_k R_{\mathrm{km}} + (1+\phi_k)\lambda_{\mathrm{rm}}}{\sqrt{1-{}^{1}\alpha}}\right] \tag{A51}$$

where

$$ \lambda_{\mathrm{rm}} = \frac{-2}{(1-b/R_{\mathrm{km}})}\left[\frac{(R_{\mathrm{km}}-1)b/R_{km}}{(1-b/R_{\mathrm{km}})^{2}} ln\left(\frac{b}{R_{\mathrm{km}}}\right) + \frac{b-1}{(1-b/R_{\mathrm{km}})} + \frac{b+1}{2}\right] \tag{A52}$$

$$ b = 1.25\left[\frac{1-{}^{1}\alpha}{{}^{1}\alpha}\right]^{10/9} \tag{A53}$$

$$ R_{\mathrm{km}} = \frac{{}^{p}k}{{}^{1}k} \tag{A54}$$

- Interphase heat transfer

$$ H_{\mathrm{gp}} = -\gamma^{0}_{\mathrm{gp}}\left({}^{p}T - {}^{1}T\right) \tag{A55}$$

where

$$ \gamma^{0}_{gp} = \frac{6\left({}^{1}_{\mathrm{Th}}k\right)(1-{}^{1}\alpha)Nu}{\left({}^{p}d\right)^{2}} \tag{A56}$$

- Nusselt number correlation

$$ Nu = \left[7-10\left({}^{1}\alpha\right)+5\left({}^{1}\alpha\right)^{2}\right]\left[1+0.7\left(Re_{p}\right)^{0.2}(Pr)^{0.33}\right]+\left[\begin{array}{c}1.33-2.4\left({}^{1}\alpha\right)\\ +1.2\left({}^{1}\alpha\right)^{2}\end{array}\right]\left(Re_{p}\right)^{0.7}(Pr)^{0.33} \tag{A57}$$

- Equation of state and sound speed of gas

$$ P = \rho RT \tag{A58}$$

$$ a = \sqrt{\frac{c_p}{c_v}RT} \tag{A59}$$

$$ N = \frac{c_v}{c_p} \tag{A60}$$

- Equation of state and sound speed of granular material

$$ P = \alpha\rho\theta\left[1+2\left({}^{p}\alpha\right)g_0(1+e)\right] \tag{A61}$$

$$ a = \sqrt{\theta\chi\left(1+\frac{2}{3}\chi+\frac{\left({}^{p}\alpha\right)}{\chi}\frac{\partial\chi}{\partial\left({}^{p}\alpha\right)}\right)}, \tag{A62}$$

- where

$$ \chi = 1+2(1+e)\left({}^{p}\alpha\right)g_0 \tag{A63}$$

$$ N\left({}^{p}\alpha, e\right) = \frac{{}^{p}\alpha\left[1+2\left({}^{p}\alpha\right)g_0(1+e)\right]}{\chi\left[1+2/3\chi+\left(\left({}^{p}\alpha\right)\chi\right)\left(\partial\chi/\partial{}^{p}\alpha\right)\right]} \tag{A64}$$

References

1. Benjamin, T.B.: Gravity currents and related phenomena. J. Fluid Mech. **31**, 209–248 (1968)
2. Britter, R.E., Simpson, J.E.: Experiments on the dynamics of gravity current head. J. Fluid Mech. **88**, 223–240 (1978)
3. Hartel, C., Meiburg, E., Necker, F.: Analysis and direct numerical simulation of the flow at a gravity current head. Part 1 Flow Topology and Front Speed for Slip and No-Slip Boundaries. J. Fluid Mech. **418**, 189–212 (2000)
4. Necker, F., Hartel, C., Kleiser, L., Meiburg, E.: High-resolution simulations of particle-driven gravity currents. Int. J. Heat Mass Trans. **28**, 279–300 (2002)
5. Bonnecaze, R.T., Huppert, H., Lister, J.R.: Particle-driven gravity currents. JFM **250**, 339–369 (1993)
6. Middleton, G.V.: Experiments on density and turbidity currents. Can. J. Earth Sci. **3**, 523–637 (1966)
7. Carey, S., et al. Pyroclastic flows and surges over water: an example from the 1883 Krakatau eruption. Bull. Volcanol. **57**, 493–511 (1996)
8. Fisher, R.V.e.a.: Mobility of a large-volume pyroclastic flow-emplacement of the Campanian ignimbrite, Italy. J. Volcanol. Geotherm. Res. **56**, 262–275 (1993)
9. Allen, S.R., Cas, R.A.F.: Transport of pyroclastic flows across the sea during explosive, rhyolitic eruption of the Kos Plateau Tuff, Greece. Bull. Volcanol. **62**, 441–456 (2001)
10. Branney, M.J., Kokelaar, P.: Pyroclastic Density Currents and the Sedimentation of Ignimbrites. The Geological Society, London (2002)
11. Freundt, A.: Entrance of hot pyroclastic flows into the sea:experimental observation. Bull. Volcanol. **65** (2003)
12. Burgisser, A., Bergantz, G.W., Breidenthal, R.E.: Addressing complexity in laboratory experiments: the scaling of dilute multiphase flows in magmatic systems. J. Volcanol. Geotherm. Res. **141**, 245–265 (2005)
13. Parsons, J.D.: Civil Engineering vol. 258. University of Illinois, Urbana–Champaign (1998)
14. Gera, D., Syamlal, M., O'Brien, T.J.: Hydrodynamics of particle segregation in fluidized beds. Int. J. Multiphase Flow **30**, 419–428 (2004)
15. Harlow, F.H., Amsden, A.A.: Numerical calculation of multiphase flow. J. Comput. Phys. **17**, 19–52 (1975)
16. Syamlal, M.: National Technical Information Service. Springfield, VA (1987)
17. Drew, D.A.: Mathematical modeling of two-phase flow. Ann. Rev. Fluid Mech. **15**, 261–291 (1983)
18. Agrawal, K., Loezos, P.N., Syamlal, M., Sundaresan, S.: The role of meso-scale structures in rapid gas-solid flows. J. Fluid Mech. **445**, 151–185 (2001)
19. Dartevelle, S., Rose, W.I., Stix, J., Kelfoun, K., Vallance, J.W.: Numerical modeling of geophysical. granular. flows: 2. Computer Simulations of Plinian Clouds and Pyroclastic Flows and Surges. GEOCHEMI. GEOPHYS. GEOSYST. **5**, 1–36 (2004)
20. Dufek, J.D., Bergantz, G.W.: Transient two-dimensional dynamics in the upper conduit of a rhyolitic eruption: A comparison of the closure models for the granular stress. J. Volcanol. Geotherm. Res. **143**, 113–132 (2005)
21. Neri, A., Dobran, F.: Influence of eruption parameters on the thermofluid dynamics of collapsing volcanic columns. JGR **99**(11), 833–11857 (1994)
22. O'Brien, T.J., Syamlal, M.: Advances in Fluidized Systems. In: Gaden, E.L., Weimer, A.W.: 127–136 (AIChE Symposium Series, pp. 127–136 (1991)
23. Parsons, J.D., Garcia, M.H.: Similarity of gravity current fronts. Phys. Fluids **10**, 3209–3213 (1998)
24. Richardson, J.F., Zaki, W.N.: Sedimentation and fluidization: Part I. Trans. Inst. Chem. Eng. **32**, 35–53 (1954)
25. Khan, A.R., Richardson, J.F.: The resistance of motion of a solid sphere in a fluid. Chem. Eng. Commun. **62**, 135–150 (1987)
26. Martin, D., Nokes, R.: Crystal settling in a vigorously convecting magma chamber. Nature **332**, 534–536 (1988)
27. Hazen, A.: On sedimentation. Trans. Am. Soc. Civil Eng. **LIII**, 45–71 (1904)
28. Crowe, C.T., Gore, R.A., Troutt, T.R.: Particle dispersion in free shear flows. Part. Sci. Tech. **3**, 149–158 (1985)
29. Raju, N., Meiburg, E.: The accumulation and dispersion of heavy particles in forced two-dimensional mixing layers. Part 2: The effect of gravity. Phys. Fluids **7**, 1241–1264 (1995)
30. Burgisser, A., Bergantz, G.W.: Reconciling pyroclastic flow and surge: the multiphase physics of pyroclastic density currents. EPSL **202**, 405–418 (2002)
31. Lun, C.K.K., Savage, S.B., Jeffrey, D.J., Chepuniy, N.: Kinetic theories for granular flow: inelastic particles in Couette flow and slighty inelastic particles in a general flow field. J. Fluid Mech. **140**, 223–256 (1984)
32. Benyahia, S., Syamlal, M., O'Brien, T.J.: Evaluation of boundary conditions used to model dilute, turbulent gas/solids flows in a pipe. Powder Technol. **156**, 62–72 (2005)
33. Jones, N.E.: An experimental investigation of particle size distribution effects in dilute gas–solid flow. PhD Thesis, Purdue University (2001)
34. Syamlal, M.: review of stress constitutive relation. (Technical Report DOE/MC/21353–2372) Department of Energy, Springfield, VA (1987)
35. Savage, S.B.: Analyses of slow high-concentration flows of granular materials. JFM **377**, 1–26 (1998)
36. Simonin, O.: Continuum modeling of dispersed two-phase flows. Combustion and Turbulence in Two-Phase Flows, Lecture Series vol. 2. Von Karman Institute of Fluid Dynamics, Rhade Saint Genèse (1996)
37. Peirano, E., Leckner, B.: Fundamentals of turbulent gas-solid flows applied to circulating fluidized bed combustion. Prog. Energy Combust. Sci. **24**, 259–296 (1998)
38. Cao, J., Ahmadi, G.: Gas-particle 2-phase turbulent-flow in a vertical duct. Int. J. Multiphase Flow **21**, 1203–1228 (1995)
39. Lowe, R.J., Linden, P.F., Rottman, J.W.: A laboratory study of the velocity structure in an intrusive gravity current. J. Fluid Mech. **456**, 33–48 (2002)
40. Syamlal, M., Rogers, W., O'Brien, T.J.: MFIX Documentation: Theory Guide, pp. 1–49. US Department of Energy, Morgantown, WV (1993)
41. Gunn, D.J.: Transfer of heat or mass to particles in fixed and fluidized beds. Int. J. Heat Mass Trans. **21**, 467–476 (1978)
42. Fedors, R.F., Landel, R.F.: An empirical method of estimating the void fraction in mixtures of uniform particles of different size. Powder Technol. **23**, 225–231 (1979)

43. Johnson, P.C., Jackson, R.: Frictional–collisional constitutive relations for granular materials, with application to plane shearing. J. Fluid Mech. **176**, 67–93 (1987)
44. Iverson, R.M.: The physics of debris flows. Rev. Geophys. **35**, 245–296 (1997)
45. Sommerfeld, M.: Analysis of collision effects for turbulent gas-particle flow in a horizontal channel: Part 1. particle transport. Int. J. Multiphase Flow **29**, 675–699 (2003)
46. Yamamoto, Y., Potthoff, M., Tanaka, T., Kajishima, T., Tsuji, Y.: Large-eddy simulation of turbulent gas-particle flow in a vertical channel: effect of considering inter-particle collisions. J. Fluid Mech. **442**, 303–334 (2001)
47. Dade, W.B., Huppert, H.E.: Runout and fine-sediment deposits of axisymmetric turbidity currents. J. Geophys. Res. **100**, 18597–18609 (1995)
48. Dade, W.B.: The emplacement of low-aspect ratio ignimbrites. J. Geophys. Res. **108**, 2211 (2003)
49. Dingman, S.L.: Fluvial hydrology. Freeman, New York (1984)
50. Ghosh, J.K., Mazumder, B.S., Saha, M.R., Sengupta, S.: Deposition of sand by suspension currents: Experimental and theoretical studies. J. Sediment. Petrol. **56**, 57–66 (1986)
51. Valentine, G.A.: Stratified flow in pyroclastic surges. Bull. Volcanol. **49**, 616–630 (1987)
52. Choux, C.M., Druitt, T.H.: Analogue study of particle segregation in pyroclastic density currents, with implications for the emplacement mechanisms of large ignimbrites. Sedimentology **49**, 907–928 (2002)
53. Burgisser, A.: Physical volcanology of the 2050 BP caldera-forming eruption of Okmok Volcano, Alaska. Bull. Volcanol. **67**, 497–525 (2004)
54. Brown, R.J., Branney, M.J.: Bypassing and diachronous deposition from density currents: evidence from a giant regressive bed form in the Poris ignimbrite, Tenerife, Canary Islands. Geology **32**, 445–448 (2004)